이학박사 학위논문

Electrical Noises in Nano-Structures and Their Correlations with Other Physical Properties Investigated via Noise Microscopy

노이즈 현미경법으로 조사한 다양한 나노 구조의 전기적 잡음 특성 및 그 특성과 나노 구조의 다른 물리적 성질들의 관계

2018 년 2 월

서울대학교 대학원

물리천문학부 물리학 전공

조 덕 형

Electrical Noises in Nano-Structures and Their Correlations with Other Physical Properties Investigated via Noise Microscopy

by

Duckhyung Cho

Supervised by

Professor Seunghun Hong

A Dissertation Submitted to the Faculty of Seoul National University in Partial Fulfillment of the Requirements for the Degree of Doctor of Philosophy

February 2018

Department of Physics and Astronomy

Graduate School

Seoul National University

Abstract

Electrical Noises in Nano-Structures and Their Correlations with Other Physical Properties Investigated via Noise Microscopy

Duckhyung Cho

Department of Physics and Astronomy

The Graduate School

Seoul National University

Electrical noise denotes a random fluctuation in an electrical signal from an electronic material or device. The generation of unwanted noises is a basic phenomenon in electronic devices and is an unavoidable problem hindering the development of reliable nanoscale electronic devices. In addition, the noise measurement and analysis can often provide important insights which are very difficult to be obtained from other methods and, thus, the study about the electrical noises is crucial for the fundamental understanding of nanoscale electronic systems. In this dissertation, it will be discussed about electrical noises in various nano-structures investigated via the variations of a noise imaging method

based on a conducting atomic force microscopy (AFM).

First, the effect of localized electrical-noise sources on the performance of perovskite-based solar cells will be discussed. Here, a photoconductive noise microscopy method was developed for the quantitative imaging of the spatial density of electrical-noise sources distributed on a solar-cell film. Interestingly, it was observed that the noise-source density had power-law relationships with local photocurrents, showing the noise-source distribution can be a key factor determining the performance of perovskite-based solar-cell films.

Second, noises in the tunneling resistance of molecular electronic junctions will be discussed. Importantly, the magnitude of the noises in molecular resistance were found to be proportional to the square of the resistance, revealing the electrical noises in the nanoscale molecular junctions mainly originate in the random fluctuation of molecule-metal bonds.

Last, the development of a vibrational noise spectroscopy (VNS) will be discussed. The VNS is a noise analysis method for the identification and imaging of the vibrational modes of molecules absorbed on conducting substrates. In VNS, a Pt probe installed on a conducting AFM was utilized to measure the electrical noises generated in molecules prepared on a conducting substrate. It was found that when

the bias voltage applied to the Pt probe matched with a vibrational mode energy of a measured molecule, the vibrational mode could be stimulated resulting in enhanced noises. Thus, by analyzing noise-voltage spectra, vibrational modes of the measured molecules could be identified. Further, the VNS could be used to image the distribution of a specific vibrational mode on the patterns comprised of different molecules.

Keywords: electrical noise, nanoelectronics, nanomaterials, atomic force microscopy, noise imaging, charge trap, vibrational spectroscopy

Student Number: 2013-30922

Table of contents

List of figures

Chapter 1

Introduction

1.1 Electrical Noise

Electrical noise is an unwanted random fluctuation in a signal, such as electrical current, from electronic devices. The noises in nanoscale electronic channels have been widely studied because they can provide a clue to understand charge transports through the nanoscale channels often exhibit completely different properties with bulk electronic channels [1,2]. In addition, the noise can be a key factor determining the reliability of a nanoscale electronic device, and thus it is essential to study the noises to realize advanced nanoelectronics based on nanoscale components [3]. The most basic and useful way to study electrical noise is to analyze the frequency characteristics of the noises [4,5]. Interestingly, in a wide variety of electronic channels, the power spectral density (S_I) of noises in DC electrical current (I) was reported to have power-law relationships with the frequency f as follows [6]:

$$S_I = A\frac{I^2}{f^\alpha} \quad (1)$$

Here, the A and α are the *noise amplitude* and *scaling parameter*, respectively [2,6]. For example, the $1/f$ noises where the α is ~ 1 have been widely reported for electronic channels based on various nanomaterials such as graphene [7], carbon nanotubes [8], and nanowires [9]. On the other hand, $1/f^2$ noises have been often reported for atomic

scale electronic junctions [10]. It has been reported that such scaling parameter, and noise amplitude also, can provide valuable information about the origin of the noise and other physical properties of the measured system [2,11]. Thus, in many cases, noise studies on electronic devices have been conducted by observing and analyzing the scaling parameter and noise amplitude.

1.2 Noise Imaging Method

Previously, noise studies on electronic channels have mainly relied on the statistical analysis of noise data obtained by measuring multiple electronic devices. However, it is a labor-intensive and time-consuming work to fabricate and measure many devices for the reliable noise analysis [12]. In addition, such device-scale noise measurements only can provide the total noise by all noise sources distributed on the measured device, and cannot provide information about the distribution or individual properties of microscopic noise sources in the device. To overcome this problem, a noise imaging method named as ‘noise microscopy’ was recently suggested by Seunghun Hong’s group [12,13]. The noise microscopy is a combined system of a conducting atomic force microscopy (cAFM), a current-noise analyzer, and a noise analysis software (Figure 1). For the noise imaging, a sharp conducting

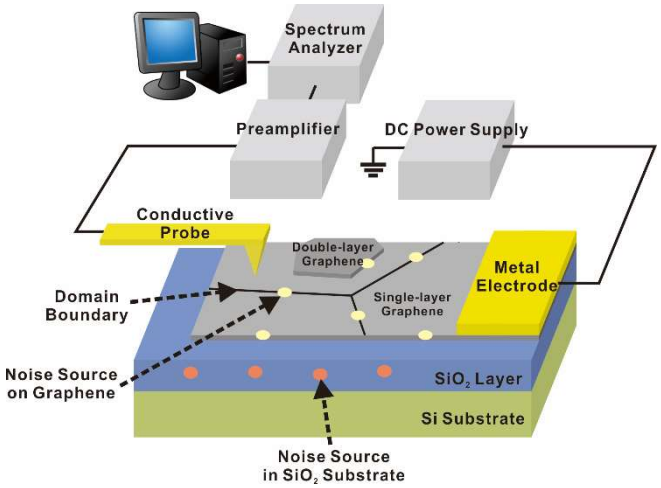

Figure 1 Schematic diagram depicting the experimental setup for the noise microscopy method on a graphene device. A Pt probe made a direct contact with a graphene sample, and it was utilized to measure the topography, electrical currents, and current noise power spectral density (PSD) simultaneously. A homemade spectrum analyzer was utilized to measure the PSD of the measured currents.

nano-probe makes a direct contact with a specific location on an electronic channel and measure local electrical currents and noises at the location. Further, by scanning the probe over the channel surface, one can obtain current and noise images showing the distribution of electrical currents and noises on the scanned area with a nanoscale resolution. Remarkably, by analyzing the noise image, one can estimate the spatial distribution of the amplitudes of electrical noises in the measured channel. Noise microscopy is a simple but powerful tool having several

advantages. For example, the noise map shows locations of the epicenters of electrical-noise generation in an electronic channel, which have been very difficult to be obtained by conventional noise measurements. Further, the noise mapping data enabled the analysis on individual properties of nanosize sources of electrical noises. With such advantages, noise imaging method is expected to open up a way to systematically study noise phenomena in nanoscale electronic channels.

1.3 References

[1] Vandamme, L. K. J. *J. Appl. Phys.* **1974,** *45*, 4563-4565.

[2] Kogan, S. *Electronic noise and fluctuations in solids*; Cambridge University Press: Cambridge, 1996.

[3] Hooge, F. N.; Kleinpenning, T. G. M.; Vandamme, L. K. J. *Rep Prog Phys* **1981,** *44*, 479-532.

[4] Sydoruk, V. A.; Xiang, D.; Vitusevich, S. A.; Petrychuk, M. V.; Vladyka, A.; Zhang, Y.; Offenhausser, A.; Kochelap, V. A.; Belyaev, A. E.; Mayer, D. *J. Appl. Phys.* **2012,** *112*, 014908.

[5] Xiang, D.; Lee, T.; Kim, Y.; Mei, T.; Wang, Q. *Nanoscale* **2014,** *6*, 13396–13401.

[6] Hooge, F. N. *Physica B & C* **1976,** *83*, 14-23.

[7] Pal, A. N.; Ghatak, S.; Kochat, V.; Sneha, E. S.; Sampathkumar, A.; Raghavan, S.; Ghosh, A. *Acs Nano* **2011,** *5*, 2075-2081.

[8] Collins, P. G.; Fuhrer, M. S.; Zettl, A. *Appl Phys Lett* **2000,** *76*, 894-896.

[9] Rajan, N. K.; Routenberg, D. A.; Chen, J.; Reed, M. A. *Ieee Electr Device L* **2010,** *31*, 615-617.

[10] Ochs, R.; Secker, D.; Elbing, M.; Mayor, M.; Weber, H. B. *Faraday Discuss.* **2006,** *131*, 281–289.

[11] Mcwhorter, A. L. *Phys Rev* **1955,** *98*, 1191-1192.

[12] Sung, M. G.; Lee, H.; Heo, K.; Byun, K.-E.; Kim, T.; Seo, D. H.;

Seo, S.; Hong, S. *ACS Nano* **2011,** *5*, 8620-8628.

[13] Lee, H.; Cho, D.; Shekhar, S.; Kim, J.; Park, J.; Hong, B. H.; Hong, S. *ACS Nano* **2016,** *10*, 10135-10142.

Chapter 2

Photoconductive Noise Microscopy on Perovskite Solar Cell

2.1 Introduction

Organic-inorganic hybrid perovskite materials have recently attracted significant interests due to their superb light-harvesting characteristics [1-9]. Over past few years, extensive efforts have been devoted to develop high-performance photovoltaic devices based on the perovskite materials, resulting in a remarkable solar cell power conversion efficiency over 20% [8]. The perovskite thin films used for the solar cell applications are typically polycrystalline ones, comprising microstructures such as grains and grain boundaries [10,11]. Therefore, the microscopic investigation and engineering of the perovskite films should be essential for the further improvement of the perovskite devices. Some pioneering researches have been performed recently to study the photoresponse of perovskite films at a microstructural level [10-13]. One of the remarkable observations in the works is that the photoresponse properties can have significant local variations even in the same perovskite film [10,12,14]. For example, the grain structures in perovskite films showed a rather large variation in the contact potential difference measurements [14]. Also, a polycrystalline perovskite film exhibited substantial grain-to-grain variations in its local photocurrents and short-circuit currents, which can significantly affect the overall performance of a solar cell device based on the film [10,12]. However,

it is still unclear about the nanostructural origin of such local variations in the solar cell performance.

In this dissertation, we developed a “photoconductive noise microscopy” method to quantitatively image localized electronic traps generating electrical noises in a photoconductive film. Then, we used the method to investigate a methylammonium lead iodide ($CH_3NH_3PbI_3$) perovskite film-based solar cell, revealing that the traps in the perovskite film can be a major factor determining the local performance of the solar cell. In this method, we mapped grain-by-grain localized electrical currents and noises on a perovskite film-based solar cell using a nanoscale conducting probe under different light conditions. Then, the maps of currents and noises were analyzed to obtain the distribution of localized photocurrents and trap densities in the solar cell film directly. We observed a large grain-by-grain variation of the local photocurrents and trap densities in the solar cell film. Importantly, the trap densities in the perovskite film were found to have power-law relationships with the local photocurrents and short-circuit currents, while the distribution of local dark currents and short-circuit currents showed no significant correlation. The results imply the traps play a significant role in the recombination of photocarriers in a perovskite film, thus determining the performance of perovskite-based solar cells. The results provide a

valuable insight on the operation of perovskite-based solar cell and an important guideline to improve its performance further.

2.2 Experimental

We prepared a $CH_3NH_3PbI_3$ perovskite film on a TiO_2 layer prepared on a fluorine doped tin oxide (FTO) substrate to form a heterojunction solar cell structure with a Pt-based atomic force microscopy (AFM) probe. For the TiO_2 layer deposition on a FTO, TiO_2 precursors of 150 mM and 300 mM titanium diisopropoxide bis(acetylacetonate) solutions (in 1-butanol) were prepared. Then, 150 mM precursor was spin-coated at 2500 rpm on FTO substrate followed by 125°C for 20 min drying. Additional spin-coating was performed identical to above using 300 mM precursor, and the substrate was finally sintered at 500°C for 30 min. Then to deposit the perovskite film, $CH_3NH_3PbI_3$ precursor solution was prepared by mixing stoichiometric CH_3NH_3I (1.2M) and PbI_2 (1.2M) in *n*,*n*-dimethylformamide at room temperature. The perovskite precursor was dropped on the TiO_2-coated FTO substrate, and spin-coating was done at 5000 rpm for 20 s. The antisolvent strategy using toluene for fast crystallization was utilized. The as-deposited perovskite film was then annealed at 120°C for 50 min. The $CH_3NH_3PbI_3$ crystal structure was

examined by x-ray diffraction (D8 Advance: Bruker), and the field-emission scanning electron microscope (Merlin Compact: Zeiss) was used to observe the surface and cross-sectional morphology.

For photocurrent and noise mapping on the prepared solar cell film, a Pt-based conducting probe (25Pt300B, Park Systems) installed on an AFM (XE-70, Park Systems) was approached and contacted to the surface of the $CH_3NH_3PbI_3$ film. Here, the contact force of the AFM probe to the film surface was maintained as 2 μN via the contact force feedback loop of the AFM system. A DC bias voltage was applied between the AFM probe and the FTO substrate using a function generator (DS345, Stanford Research Systems), and current signals through the probe were measured and amplified by a low-noise preamplifier (SR570, Stanford Research Systems) connected to the probe. The amplified current signals were filtered by a band-pass filter included in the preamplifier to obtain the electrical noise signal which is the fluctuating component of the current signals. The RMS power of the noise signal could be obtained using a RMS-to-DC converter built using an AD737 chip (purchased from Analog Devices). Note that the obtained noise power is the integrated value of the noise PSDs over the frequency range of the pass band of the used band-pass filter. Finally, we get the noise PSD value at the central frequency of the pass band, by dividing

the measured noise power with the bandwidth of the band-pass filter. By scanning the AFM probe while measuring both current and noise PSD on the $CH_3NH_3PbI_3$ film surface, we could obtain the current and noise PSD maps simultaneously. Further, we measured a current map while illuminating a white light to the film using a light source (LS-F100HS) and compared the map with that obtained at a dark condition to obtain a photocurrent map.

2.3 Photoconductive Noise Microscopy Setup

Figure 2-1a in the next page shows the schematic diagram showing our experimental setup for the imaging of charge traps and local photocurrents on a $CH_3NH_3PbI_3$ perovskite film-based solar cell. The details about the solar cell fabrication and photoconductive noise microscopy set-up are described in the experimental section. In brief, the $CH_3NH_3PbI_3$ perovskite film of ~400 nm thickness was prepared on a compact TiO_2 layer on a fluorine doped tin oxide (FTO)-coated glass via a solution-based antisolvent strategy [15-17]. Thus, a $CH_3NH_3PbI_3$-

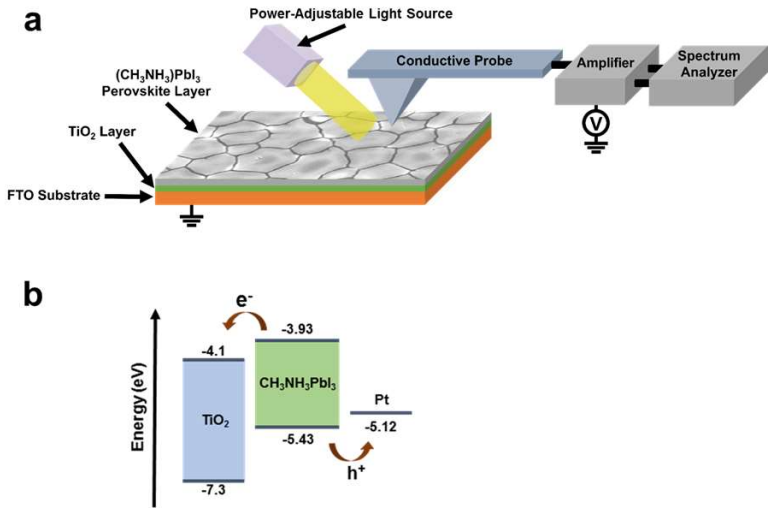

Figure 2-1 Photoconductive noise microscopy set-up and the energy levels of a $CH_3NH_3PbI_3$-based heterojunction solar cell film. (a) Experimental set-up for photoconductive noise microscopy measurements on a $CH_3NH_3PbI_3$ perovskite film. (b) Energy level diagram of a $CH_3NH_3PbI_3/TiO_2$ heterojunction solar cell.

TiO_2 heterojunction solar cell structure was formed, and the $CH_3NH_3PbI_3$ layer acted as a photo-reactive layer as well as a hole conducting layer [14,18,19]. The FTO layer worked as an electron-collecting electrode, and the TiO_2 layer on the FTO film acted as a hole blocking layer [18]. Then, a Pt-based conducting probe installed on a conductive AFM was contacted to the perovskite film and used as a nanosize hole-collecting electrode. Further, we combined a power-adjustable light source with the AFM, for photoconductive noise microscopy measurements [20,21]. While operating the solar cell film

with light illumination and a bias voltage, the current signals through the probe was measured and amplified by a preamplifier connected to the probe. The measured current can show the 'local current generation' of the solar cell film at the location of the probe. Simultaneously, a noise component in the localized current was measured using a home-built noise spectrum analyzer comprising a band-pass filter and a RMS-to-DC converter [22]. By scanning the probe over the sample area, we were able to obtain the maps of the localized photocurrents and current noises. The measured noise map was analysed to calculate the distribution of charge traps. By comparing the current and noise maps measured under the dark and illuminated conditions, we could obtain the maps showing the distribution of local photocurrents and current noise changes in the solar cell film.

Figure 2-1b is the energy-level diagram of the $CH_3NH_3PbI_3/TiO_2$ heterojunction solar cell structure. The diagram shows the conduction-band minimum (CBM) and the valence-band maximum (VBM) of $CH_3NH_3PbI_3$ and TiO_2. When the $CH_3NH_3PbI_3$ layer absorbs lights, valence electrons are excited into the conduction band, leaving holes in the valence band. The excited electrons at the CBM of the $CH_3NH_3PbI_3$ (-3.93 eV vs. vacuum) pass into the TiO_2 layer which has a lower CBM (-4.10 eV) compared to the $CH_3NH_3PbI_3$. The

holes at the VBM of the $CH_3NH_3PbI_3$ are injected into the Pt-based conducting AFM probe. The *TiO_2 layer* and *the bottom FTO substrate* act as *a hole-blocking layer* and *an electron collector*, respectively. Such $CH_3NH_3PbI_3/TiO_2$ heterojunction structure with FTO and metal contacts has been reported to be very efficient in harvesting light energies, and also is useful in studying the basic characteristics of $CH_3NH_3PbI_3$ due to its simple structure without an additional hole-transport layer [14,18,19].

2.4 Properties of $CH_3NH_3PbI_3/TiO_2$ Heterojunction Structures

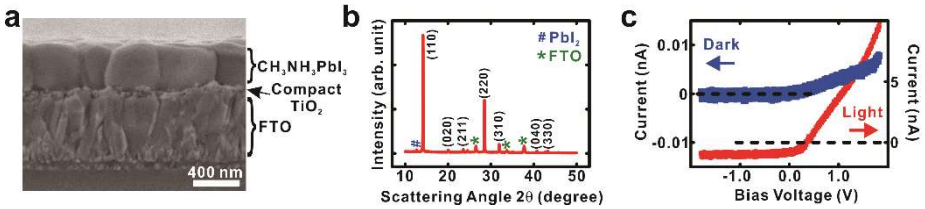

Figure 2-2 Characterization of a $CH_3NH_3PbI_3/TiO_2$ heterojunction solar cell structure. (a) Scanning electron microscope image showing the vertical structure of $CH_3NH_3PbI_3/TiO_2$ layers on a FTO substrate. (b) X-ray diffraction results of the sample. (c) *I-V* curves measured on the sample with (red line) and without (blue line) a light illumination via the photoconductive noise microscopy.

The scanning electron microscopy (SEM) image in Figure 2-2a shows well-defined interfaces between $CH_3NH_3PbI_3$ and the compact TiO_2

layer with the uniform thickness of perovskite, demonstrating the high quality of the heterojunction solar cell film. Also, Figure 2-2b shows the x-ray diffraction (XRD) spectroscopy results of the $CH_3NH_3PbI_3$ film. The data show strong $CH_3NH_3PbI_3$ (110) peaks and the negligible residual PbI_2, indicating the purity of the $CH_3NH_3PbI_3$ film.

Figure 2-2c shows the current-voltage curves of the solar cell film measured with (red line) and without (blue line) the illumination of a white light with its power density of 100 mW/cm^2. Here, we measured electrical currents (I) through the $CH_3NH_3PbI_3/TiO_2$ between the conducting probe at a bias voltage (V) and the electrically-grounded FTO substrate. In the dark condition, a typical asymmetric I-V curve of a p-n junction was observed. When the film was illuminated with the light, the current level was increased significantly compared to the dark condition, indicating the significant generation of photocarriers in the $CH_3NH_3PbI_3$ film. In addition, a short-circuit photocurrent of ~1 nA was observed at the zero-bias condition, indicating the successful collection of the photocarriers in our $CH_3NH_3PbI_3/TiO_2$ heterojunction solar cell structure with the Pt probe.

2.5 Imaging of Electronic Traps on a Perovskite Solar

Cell via Photoconductive Noise Microscopy

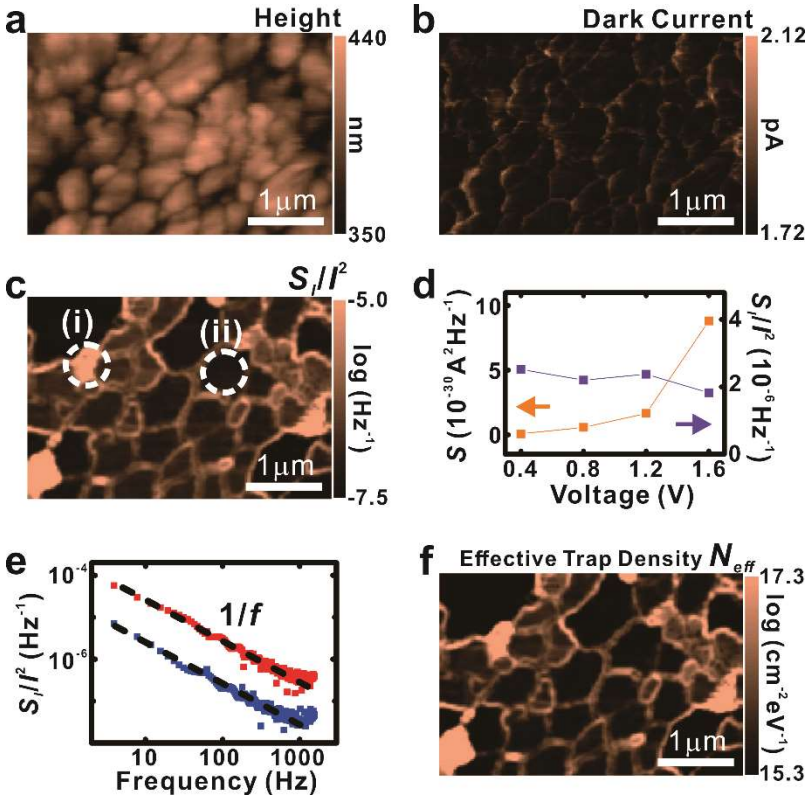

Figure 2-3 Noise microscopy measurements on a $CH_3NH_3PbI_3$ perovskite film in a solar cell structure. (a) AFM topography image. (b) Dark current map (at 1.6 V) measured simultaneously with the topography image. (c) Map showing the distribution of current-normalized noise power spectral density S_I/I^2 (at 170 Hz). (d) Noise power spectral density S_I and current-normalized noise power spectral density S_I/I^2 values (at 170 Hz) measured with different bias voltages under dark conditions. The S_I/I^2 values were nearly constant regardless of the voltage, implying the noises were generated mainly via the carrier number fluctuation. (e) Frequency spectra of S_I/I^2 which were measured at two different locations. *Red* and *blue* data were the spectra measured at *(i)* and *(ii)* in Figure

2-3c, respectively. (f) Effective trap density (N_{eff}) map calculated from the S_I/I^2 map. A large grain-by-grain variation of the trap density was observed.

Figure 2-3a shows an AFM topography image of a $CH_3NH_3PbI_3$ film on a TiO_2/FTO layer in the solar cell structure. The contact force of the conducting AFM probe to the film surface was maintained as 2 μN during the AFM scanning. The topography image shows that the $CH_3NH_3PbI_3$ film consisted of adjoined small $CH_3NH_3PbI_3$ grains. The sizes of individual grains varied between 500 and 1000 nm laterally in their diameters, which are as large as the film thickness. The SEM image in Figure 2-2a clearly shows that individual grains extended throughout the film in a vertical direction without any grain boundaries, which is also consistent with previous reports [14,23].

A localized current map in a dark condition was measured simultaneously with the topography image (Figure 2-3b). To measure the dark current map, a DC bias voltage of 1.6 V was applied to the conducting probe, and the FTO substrate was electrically grounded. Then, the current through the AFM probe was recorded while the probe scanned over the film surface to obtain the current map. The result shows that the overall region of the $CH_3NH_3PbI_3$ film was conductive, and the average current level was ~1.8 pA under the dark condition. The

boundaries of $CH_3NH_3PbI_3$ grains identified in the topography map exhibited rather high current levels compared with the interior regions of individual grains, which could be attributed to the thinner film thickness near the grain boundaries. The localized current could be successfully mapped for the whole scanned area, indicating that the conducting AFM probe and the film surface made a stable electrical contact regardless of the topological roughness of the film, which should be essential for the reliable current and noise measurements. Since the resistance of the $CH_3NH_3PbI_3$ film is much higher than that of the FTO, we can assume that charge carriers mainly flowed in a vertical direction from the underlying FTO substrate to the AFM probe passing through the perovskite layer [14,24,25]. In such a case, currents flowing in the lateral direction along the film surface are negligible, and various noise sources inside or on the perovskite film can be responsible for the measured noises [14,24,25].

The current-normalized noise power spectral density (S_I/I^2) value can be a useful parameter to represent the electrical-noise level of an electronic channel [24]. Figure 2-3c shows the map of S_I/I^2 (at 170 Hz) estimated from the noise power spectral density (PSD) map measured simultaneously with the current map under a dark condition. Here, we first measured the map of noise PSD (S_I) at 170 Hz via the noise

microscopy, and divided the measured S_I map by the square of the current map to obtain the S_I/I^2 map. Note that the S_I/I^2 level varied significantly between grains, while it did not vary much inside each individual grain. For example, a grain marked with (i) in the Figure 2-3c showed the S_I/I^2 value of ~3×10^{-6} Hz^{-1} which is ~40 times higher than the S_I/I^2 value of ~7×10^{-8} Hz^{-1} in the grain marked with (ii). Interestingly, the dark current map (Figure 2-3b) and the noise map (Figure 2-3c) do not show any correlations, implying that the noise sources in the $CH_3NH_3PbI_3$ film did not affect its dark conductivity. This is a noteworthy observation considering that noise sources in many of the electronic materials seriously degrade their conductivity [24]. Previously, it was suggested that the charge-carrier scattering in a polycrystalline perovskite film is dominated by the *lattice scattering* (phonon scattering), while the main carrier scattering mechanism in many other amorphous electronic materials can be the impurity scattering [26]. In the case of the lattice scattering, impurities like deep levels or charge traps, which often work as noise sources, might not much degrade the carrier mobility or the conductivity, which is consistent with our observation [26].

Figure 2-3d shows S_I and S_I/I^2 (at 170 Hz) measured in a grain marked by *(i)* in Figure 2-3c with different bias voltages under the dark condition. Note that the S_I values increased as the bias-voltage increased.

However, the S_I/I^2 values were nearly constant regardless of the applied voltage. It was previously reported that the main intrinsic source of low-frequency noise in perovskite films is charge traps generating carrier-number fluctuations [27-29] and the measured S_I/I^2 values in a conducting channel can be utilized to estimate the concentration of such noise sources [24,27]. Our observation indicates the measured S_I/I^2 values measured in our solar cell film are not much affected by external bias voltages and thus can be used to estimate the noise source densities representing the intrinsic properties of the film.

Figure 2-3e shows the S_I/I^2 spectra which were measured at two different locations on the film. Here, the probe (biased at 1.6 V) was in a contact with a specific position on the $CH_3NH_3PbI_3$ film, and the electrical currents through the conducting AFM probe were measured and analyzed using a fast Fourier transform (FFT) signal analyzer (SR770, Stanford Research Systems). The noise PSD versus frequency (*f*) spectra measured at locations indicated by *(i)* and *(ii)* in Figure 2-3c were represented by *red* and *blue* symbols, respectively. The slopes of the both curves were close to ~1, indicating *1/f* noise behaviors of the $CH_3NH_3PbI_3$ film. Those behaviors are consistent with the known *1/f* noise behavior of a polycrystalline perovskite film [30]. In our previous works about electrical noises using nanoscale probes, we showed that

when the electrical noises were mainly generated by a small number of noise sources in the nanoscale tip-substrate contact area on the substrate surface, the frequency spectra of the noise PSDs exhibited a $1/f^2$ behavior [31-33]. And, the behavior was attributed to rather uniform characteristic trapping times of such a small number of noise sources in the nanoscale contact regions. On the other hand, when electrical noises were generated by a rather large number of noise sources with a rather large variation of characteristic trapping times, we observed a $1/f$ noise behavior [31-33]. The $1/f$ behavior in our result indicates that the electrical noises were mainly generated by a rather large number of noise sources inside the perovskite films.

We developed a method to quantitatively estimate the density of localized charge traps in a perovskite film using the measured S_I/I^2 map. In this method, we assumed that the measured $1/f$ noises in the perovskite-based solar cell junction were generated by the carrier-number fluctuation in the perovskite film layer, as suggested by a previous report [30]. Because the capture and release of charge carriers by a trap are random processes, the number of traps occupied by the carrier fluctuates randomly with time, generating electrical noises [32,33]. At a dark condition, the perovskite layer has a much higher resistivity than the TiO_2 layer [34,35]. In addition, at a high forward bias

condition, the voltage drop at the diode contact between the perovskite/TiO_2 junction should be much smaller than that at the highly-resistive perovskite layer. Thus, we could assume that the most of voltage drops occurred at the perovskite layer in our solar cell structure at a dark condition with a high forward bias voltage. Then, let's consider a conducting AFM probe in contact with a $CH_3NH_3PbI_3$ perovskite film surface at a position of (x, y) on the film surface. The noise PSD of the number of occupied traps (S_{Nt}) in the small $CH_3NH_3PbI_3$ film segment in contact with the probe can be written like [32,36,37],

(1) $$S_{N_t}(f,x,y) = \Delta x \Delta y \int_{-\infty}^{\infty} \int \frac{4\tau(E,x,y,z)}{1+[2\pi f \cdot \tau(E,x,y,z)]^2} \cdot f_t(1-f_t) \cdot N_t(E,x,y,z)\ dz\ dE$$

where the N_t, f_t, f, and τ are the *density of traps over space and energy*, the trap *occupancy function*, a *frequency*, and a *trapping time constant*, respectively. The integration in the z direction (vertical direction to the film surface) ranges from *0* to the thickness of the $CH_3NH_3PbI_3$ film. At room temperature, f_t (1-f_t) behaves like a delta function around the Fermi level, and Eq. (1) after the integration over electron energy E can be written as [38]

(2) $S_{N_t}(f,x,y) =$

$$\Delta x \Delta y \cdot kT \cdot \int \frac{4\tau(E_f, x, y, z)}{1 + [2\pi f \cdot \tau(E_f, x, y, z)]^2} \cdot N_t(E_f, x, y, z) \cdot dz$$

Here, we define the effective trap density N_{eff} like

(3) $$N_{eff}(f, x, y) \equiv f \cdot \int \frac{4\tau(E_f, x, y, z)}{1+[2\pi f \cdot \tau(E_f, x, y, z)]^2} \cdot N_t(E_f, x, y, z) \cdot dz$$

Then, Eq. (2) can be simply rewritten as

(4) $$S_{N_t}(f, x, y) = \frac{kT}{f} N_{eff}(f, x, y) \cdot \Delta x \Delta y$$

with the charge carrier number ΔC in the area $\Delta x \Delta y$ and the electrical current I through the small segment of the $CH_3NH_3PbI_3$ film, we can write the PSD of the current noises generated by the segment as [32]

(5) $$S_I(f, x, y) = \frac{(I)^2}{(\Delta C)^2} S_{N_t}(f, x, y) = \frac{(I)^2}{(\Delta C)^2} \frac{kT}{f} N_{eff}(f, x, y) \ \Delta x \Delta y$$

Then, N_{eff} can be written as

(6) $$N_{eff}(f, x, y) = \frac{(\Delta C)^2}{(I)^2} \frac{f}{kT} \cdot \frac{S_I(f, x, y)}{\Delta x \Delta y}$$

It is worth discussing a few interesting aspects of the N_{eff}. First, in the case of $1/f$ noise, S_I at a (x, y) position is proportional to $1/f$. Thus, $S_I \times f$ is constant at a position (x, y), and $N_{eff}(f, x, y)$ can be expressed as $N_{eff}(x, y)$. Furthermore, considering that the N_{eff} is the integrated value of the trap density over the z-direction, it can be a convenient value to represent the effective number of charge traps per unit area in a two-dimensional film. Utilizing Eq. (6), we calculated the map of the effective trap density

N_{eff} from the S_I/I^2 map in Figure 2-3c (Figure 2-3f). For the calculation, we used the $\Delta x\ \Delta y$ value of ~100 nm^2 which is the effective contact area of our conducting AFM probe provided by the manufacturer. For ΔC, we used a reported value (~10^{18} cm^{-3}) of carrier concentrations in a $CH_3NH_3PbI_3$ film [39]. The calculated N_{eff} map shows the non-uniform distribution of traps over the film (Figure 2-3f). The N_{eff} inside individual grains ranges from 10^{15} to 10^{16} $cm^{-2}eV^{-1}$. In the grain boundary regions, the trap density was distinctively high reaching ~10^{17} $cm^{-2}eV^{-1}$, presumably due to the disordered nature of the boundary regions. The charge trap distribution has been believed to significantly affect the photovoltaic characteristics of a photoreactive film, and extensive research efforts have been devoted to study such traps [40]. However, until now, it has been very difficult, if not impossible, to image the nanoscale distribution of charge traps in a photoreactive film. Thus, our results should be a significant breakthrough in the research on a perovskite film and show the versatility of our noise mapping method. It is also worth mentioning the possible applications and limitations of our method. Since our method can be applied to various conducting substrates, as long as a nanoscale conducting probe can make a good electrical contact on their surfaces, it can be applied to diverse optoelectronic devices based on various materials such as conducting

polymers and graphene [24,31,33]. However, for some conducting materials with a rather thick surface oxide layer under ambient conditions, the measurement may have to be done under vacuum environments.

2.6 Effect of Trap Distribution on Local Performance

of Perovskite Solar Cell

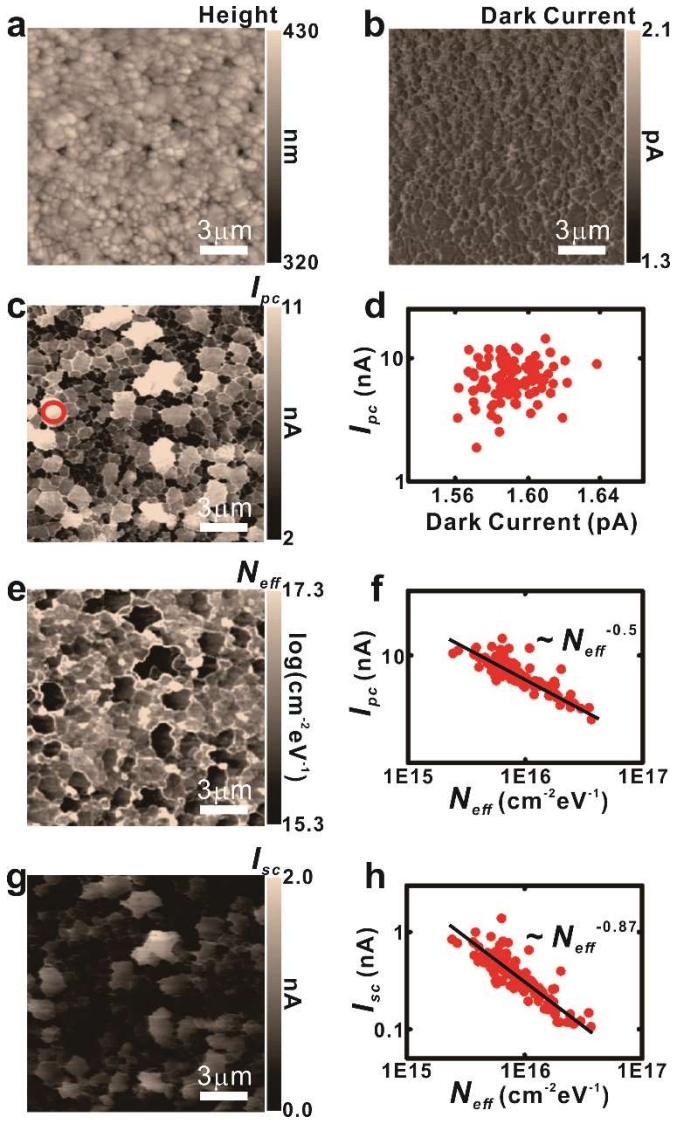

Figure 2-4 Mapping of local photocurrents and short-circuit currents (with illumination) over a 15×15 μm^2 region of a $CH_3NH_3PbI_3$ perovskite film in a solar cell structure. (a) AFM topography image. (b) Dark current map at 1.6 V (without illumination). (c) Photocurrent map at 1.6 V showing large local variations of the photocurrents between grains. (d) Scattered plot of dark currents vs. photocurrents. Each point represents the averaged values of the

measured dark current and photocurrent data over a single grain. (e) Map of the effective trap density (N_{eff}) distribution. (f) Scattered plot showing the relation between the trap density N_{eff} and the photocurrent. Each point represents the averaged values of the measured data over a single grain. The photocurrents are inversely proportional to the square root of the trap densities. (g) Map of the short-circuit current measured without an external bias. (h) Scattered plot showing the relation between the trap density and the short-circuit current. Each point represents the averaged values of the measured data over a single grain. The short-circuit currents were inversely proportional to the 0.87 power of the trap densities.

To further study the effect of the charge trap distribution on the local photovoltaic characteristics of the $CH_3NH_3PbI_3$ film, we imaged a rather large area of the film under different illumination and bias conditions (Figure 2-4). Figure 2-4a,b show topography and dark current maps measured over a 15×15 μm^2 region of the $CH_3NH_3PbI_3$ film. The topography map shows more than a hundred of different topological grains in the region. The dark current map was measured under the dark condition with a DC bias voltage of 1.6 V. The dark current level was quite uniform throughout the whole region, and grain boundary regions showed a bit higher dark current level compared to the intragrain regions, presumably due to the thinner film thickness at the grain boundaries.

Figure 2-4c shows the photocurrent map in the same region on the perovskite film. Here, a current map was measured at 1.6 V with the

light illumination of 100 mW/cm^2, and it was subtracted by the dark current map (Figure 2-4b) to obtain the photocurrent map. The photocurrent map exhibited distinctive grains whose shapes are a bit different from those in the topological image or the dark current map. More than a hundred of grains can be clearly identified with their averaged photocurrent level of ~7 nA. Interestingly, the photocurrent level varied significantly between grains in the film, while the dark current in Figure 2-4b appeared to be nearly uniform.

Figure 2-4d is a scatter plot of the dark current and photocurrent level in individual grains. Here, we utilized an image processing method based on the Sobel algorithm [41,42] to identify the grain boundary regions where the photocurrent level was abruptly changed in the photocurrent map. Then, the averaged values of dark currents and photocurrents of ~100 identified grains were calculated. Each data point in the Figure 2-4d shows the averaged value of dark currents and photocurrents in a single grain identified by the Sobel method. In the plot, we could not observe a significant correlation between the dark current and the photocurrent, which clearly shows that the photoconduction of a perovskite film has no direct relation with its dark resistivity. Previously, it was suggested that the photoconduction in perovskite films could be significantly affected by various nanostructures such as charge traps in

them [3,40,43]. On the other hand, their resistivity under a dark condition is suggested to be mainly determined by the lattice structures of the film rather than the traps, which is consistent with our results [26].

Figure 2-4e shows the effective trap density N_{eff} map obtained from a S_I/I^2 map (at 170 Hz) measured simultaneously with the dark current map in Figure 2-4b. Note that the grains with a high trap density N_{eff} in Figure 2-4e exhibited a rather low photocurrent level in Figure 2-4c. This result clearly shows that the charge traps can degrade the photoconduction in a perovskite film.

Figure 2-4f shows a scatter plot showing the relation between the trap density and photocurrent level of grains in the $CH_3NH_3PbI_3$ film. Each data point shows the averaged photocurrent and trap density values of a single grain identified by the Sobel method. Here, we can observe a negative correlation between the trap density and the photocurrent level. On the other hand, there was no clear correlation between the trap density and dark current. More specifically, the photocurrent level was found to be inversely proportional to the *0.5* power of the trap density. The observation directly shows that the charge trap density N_{eff} can be a dominant parameter determining local I_{pc} on a perovskite film. One plausible explanation for this result can be a trap assisted recombination process of photocarriers in a perovskite film [40,44]. When a perovskite

film was illuminated with a light, the film can absorb photons to generate electron-hole pairs increasing the number of charge carriers, and the photocurrent I_{pc} at a high-forward bias condition should be proportional to the number of generated photocarriers. Previous studies suggested that the traps can assist the recombination of photo-generated electrons/holes and thus reduce the number of photocarriers. In this case, the trap-assisted recombination rate (r_{recomb}) of photocarriers in an illuminated perovskite film could be written like [45]

$$(7) \quad r_{recomb} = C_n C_p N_{eff}(pn - p_1 n_1)/\left[C_n(n - n_1) + C_p(p - p_1)\right]$$

where C_n and C_p are the capture coefficients of traps for *electrons* and *holes*, respectively. The n and p are the volume density of *electrons* and the *holes* including photo-generated ones, respectively. The n_1 and p_1 are the *electron* and *hole* densities in the dark condition, respectively. In our $CH_3NH_3PbI_3$ film, the photocurrents were 1000 times larger than the dark currents, and thus the total carrier numbers (p and n) under the illumination were much larger than the intrinsic carrier numbers (p_1 and n_1) under the dark condition. Further, the numbers of photo-generated electrons and holes could be assumed to be identical (as ~n), because they are always generated as a pair by absorbed photons. Then, Eq. (7) could be approximated as

(8) $$r_{recomb} = \frac{C_n C_p}{(C_n + C_p)} N_{eff} n$$

Here, the $C_nC_p/(C_n+C_p)$ is a constant which is independent to the N_{eff} and n. Previous literatures suggested that n or r_{recomb} is *proportional* or *inversely-proportional* to the photocarrier lifetime [46,47]. In this case, we can write like

(9) $$r_{recomb} \propto \frac{1}{n}$$

By combining Eq. (8, 9), we can expect the correlation between the photocurrent and trap densities like

(10) $$n \propto \frac{1}{(N_{eff})^{0.5}} \propto I_{pc}$$

Eq. (10) suggests that the n as well as the photocurrent I_{pc} is inversely proportional to 0.5 power of N_{eff}, which is consistent with our experimental observation in Figure 2-4f. Thus, our observation on the strong N_{eff}-I_{pc} correlation suggests that the charge traps generating electrical noises can reduce the photocarriers via the trap-assisted recombination mechanism, resulting in the degraded photoconduction of perovskite films [44].

The short-circuit current is an important parameter to estimate the efficiency of a solar cell. Figure 2-4g shows a short-circuit current map showing the distribution of local short-circuit current on the perovskite film. With illuminating a white light with a power density of

100 mW/cm^2, we mapped the currents with a zero bias voltage. The average level of the short-circuit current was ~0.4 nA, which is comparable to a previously-reported value of perovskite-based solar cells [48]. Interestingly, the map showed a large grain-by-grain variation of the short-circuit current level. Comparing the short-circuit current map (Figure 2-4g) with the N_{eff} map (Figure 2-4e), one can clearly see the strong negative correlation between the local short-circuit current and the trap density in the $CH_3NH_3PbI_3$ film. Previously, it was suggested that the traps in a perovskite film could act as a recombination center of photocarriers and degrade the solar-cell performance. Our result indicates that charge traps can degrade the performance of a solar cell device based on the perovskite films.

Figure 2-4h shows a scatter plot showing the relation between the trap density and short-circuit current level of individual grains in the $CH_3NH_3PbI_3$ film. Each data point represents the short-circuit current and trap density values of a single grain identified by the Sobel method. The results show that the short-circuit currents were approximately *inversely proportional* to the *0.87* power of the trap densities, as indicated with a least-square fitting line. Considering that the photocurrent was found to be inversely proportional to the square root of the trap density, the results confirm that the short-circuit current was

affected more sensitively by the trap density than the case of the high-bias photocurrent. In the short-circuit condition where the external voltage source was removed, the photocarriers in a solar cell should diffuse to the electrodes to generate a short-circuit current. In this case, the short-circuit current (I_{sc}) in the solar cell should be proportional to the multiplication of the generation rate of photocarriers (G) and the photocarrier collection length (L_c) of the solar cell like [49]

(11) $$I_{sc} \propto (G \times L_c)$$

Note that the G is proportional to the photocarrier density (n) which is inversely proportional to the $N_{eff}^{0.5}$ as Eq. (10) [49]. On the other hand, the L_c is approximately equal to the sum of the depletion width and the carrier diffusion length (L_D) of the photoreactive layer in the solar cell [50]. Because the depletion width of our $CH_3NH_3PbI_3/TiO_2$ heterojunction solar cell structure is much smaller than the diffusion length [6,19], L_c can be assumed to be identical to L_D. L_D is known to be proportional to the square root of the carrier lifetime (τ) as [51],

(12) $$L_D = \sqrt{D\tau}$$

where D is a carrier diffusivity. Since the carrier density n and τ are inversely proportional to the $N_{eff}^{0.5}$, the L_D should be inversely proportional to the $N_{eff}^{0.25}$. Then, from Eq. (11), the short-circuit current

I_{sc} can be expected to be inversely proportional to the $N_{eff}^{0.75}$. This behavior agrees well with the measured result of $I_{sc} \sim N_{eff}^{0.87}$ in Figure 2-4h, indicating the observed N_{eff}-I_{sc} relation can be consistently explained by the trap-assisted recombination model. Our results suggest that charge traps in a perovskite film can significantly reduce the photocarrier lifetime via the trap-assisted recombination mechanism and, in effect, degrade the local performances of a perovskite-based solar cell, which can be a key information in designing efficient light-harvesting devices in the future.

2.7 Summary

In summary, we developed a photoconductive noise microscopy method, and applied the method to image the trap distribution and local photocurrents on a $CH_3NH_3PbI_3$ perovskite film in a solar cell structure. Interestingly, we observed that local photocurrent and trap density varied significantly between individual grains in the film, and the trap density and photocurrent level of a grain had a power-law relationship. These results imply that the charge traps generating electrical noises in a perovskite film can significantly affect the photocarrier recombination via the trap-assisted recombination mechanism. Further, we observed

that the short-circuit current level of a $CH_3NH_3PbI_3$ grain was inversely proportional to the 0.87 power of the trap density, revealing the trap distribution can be the major factor governing the local performance of perovskite-based solar cells. These results should provide an important guideline in developing more efficient solar cell devices based on the perovskite films. Since our novel methods allow us to easily map the effect of charge traps on the versatile photoresponses on a solar cell film, it can be a powerful tool for both basic researches and industrial applications of photoelectronic devices.

2.8 References

[1] McMeekin, D. P.; Sadoughi, G.; Rehman, W.; Eperon, G. E.; Saliba, M.; Hörantner, M. T.; Haghighirad, A.; Sakai, N.; Korte, L.; Rech, B.; Johnston, M. B.; Herz, L. M.; Snaith, H. J. *Science* **2016,** *351*, 151-155.

[2] Burschka, J.; Pellet, N.; Moon, S.-J.; Humphry-Baker, R.; Gao, P.; Nazeeruddin, M. K.; Grätzel, M. *Nature* **2013,** *499*, 316-319.

[3] Zhou, H.; Chen, Q.; Li, G.; Luo, S.; Song, T.-B.; Duan, H.-S.; Hong, Z.; You, J.; Liu, Y.; Yang, Y. *Science* **2014,** *345*, 542-546.

[4] Malinkiewicz, O.; Yella, A.; Lee, Y. H.; Espallargas, G. M.; Graetzel, M.; Nazeeruddin, M. K.; Bolink, H. J. *Nat. Photonics* **2014,** *8*, 128-132.

[5] Xiao, Z.; Yuan, Y.; Shao, Y.; Wang, Q.; Dong, Q.; Bi, C.; Sharma, P.; Gruverman, A.; Huang, J. *Nat. Mater.* **2015,** *14*, 193-198.

[6] Stranks, S. D.; Snaith, H. J. *Nat. Nanotechnol.* **2015,** *10*, 391-402.

[7] Nie, W.; Tsai, H.; Asadpour, R.; Blancon, J.-C.; Neukirch, A. J.; Gupta, G.; Crochet, J. J.; Chhowalla, M.; Tretiak, S.; Alam, M. A.; Wang, H.-L.; Mohite, A. D. *Science* **2015,** *347*, 522-525.

[8] Saliba, M.; Matsui, T.; Domanski, K.; Seo, J.-Y.; Ummadisingu, A.; Zakeeruddin, S. M.; Correa-Baena, J.-P.; Tress, W. R.; Abate, A.; Hagfeldt, A.; Grätzel, M. *Science* **2016,** *354*, 206-209.

[9] Eames, C.; Frost, J. M.; Barnes, P. R. F.; O'Regan, B. C.; Walsh, A.; Islam, M. S. *Nat. Commun.* **2015,** *6*, 7497.

[10] Kutes, Y.; Zhou, Y.; Bosse, J. L.; Steffes, J.; Padture, N. P.; Huey, B. D. *Nano Lett.* **2016,** *16*, 3434-3441.

[11] Leblebici, S. Y.; Leppert, L.; Li, Y.; Reyes-Lillo, S. E.; Wickenburg, S.; Wong, E.; Lee, J.; Melli, M.; Ziegler, D.; Angell, D. K.; Ogletree, D. F.; Ashby, P. D.; Toma, F. M.; Neaton, J. B.;

Sharp, I. D.; Weber-Bargioni, A. *Nat. Energy* **2016,** *1*, 16093.

[12] Li, J.-J.; Ma, J.-Y.; Ge, Q.-Q.; Hu, J.-S.; Wang, D.; Wan, L.-J. *ACS Appl. Mater. Interfaces* **2015,** *7*, 28518-28523.

[13] Zhao, Z.; Chen, X.; Wu, H.; Wu, X.; Cao, G. *Adv. Funct. Mater.* **2016,** *26*, 3048–3058.

[14] Yun, J. S.; Ho-Baillie, A.; Huang, S.; Woo, S. H.; Heo, Y.; Seidel, J.; Huang, F.; Cheng, Y.-B.; Green, M. A. *J. Phys. Chem. Lett.* **2015,** *6*, 875-880.

[15] Hwang, T.; Cho, D.; Kim, J.; Kim, J.; Lee, S.; Lee, B.; Kim, K. H.; Hong, S.; Kim, C.; Park, B. *Nano Energy* **2016,** *25*, 91-99.

[16] Lee, B.; Lee, S.; Cho, D.; Kim, J.; Hwang, T.; Kim, K. H.; Hong, S.; Moon, T.; Park, B. *ACS Appl. Mater. Interfaces* **2106,** *8*, 30985-30991.

[17] Jeon, N. J.; Noh, J. H.; Kim, Y. C.; Yang, W. S.; Ryu, S.; Seok, S. I. *Nat. Mater.* **2014,** *13*, 897-903.

[18] Etgar, L.; Gao, P.; Xue, Z.; Peng, Q.; Chandiran, A. K.; Liu, B.; Nazeeruddin, M. K.; Grätzel, M. *J. Am. Chem. Soc.* **2012,** *134*, 17396-17399.

[19] Laban, W. A.; Etgar, L. *Energy Environ. Sci.* **2013,** *6*, 3249-3253.

[20] Coffey, D. C.; Reid, O. G.; Rodovsky, D. B.; Bartholomew, G. P.; Ginger, D. S. Nano Lett. 2007, 7, 738–744.

[21] Dang, X.-D.; Tamayo, A. B.; Seo, J.; Hoven, C. V.; Walker, B.; Nguyen, T.-Q. *Adv. Funct. Mater.* **2010,** *20*, 3314–3321.

[22] M. Engelson, *Modern spectrum analyzer theory and applications*; Artech House: Norwood, 1984.

[23] Zhou, Y.; Game, O. S.; Pang, S.; Padture, N. P. *J. Phys. Chem. Lett.* **2015,** *6*, 4827−4839.

[24] Shashank, S.; Cho, D.; Lee, H.; Cho, D.-G.; Hong, S. *Nanoscale* **2016,** *8*, 835-842.

[25] Chen, Y.; Peng, J.; Su, D.; Chen, X.; Liang, Z. *ACS Appl. Mater. Interfaces* **2015,** *7*, 4471−4475.

[26] Karakus, M.; Jensen, S. A.; D'Angelo, F.; Turchinovich, D.; Bonn, M.; Cánovas, E. *J. Phys. Chem. Lett.* **2015,** *6*, 4991-4996.

[27] Macku, R.; Koktavy, P. *Phys. Status Solidi A* **2010,** *207*, 2387-2394.

[28] Fang, Y.; Dong, Q.; Shao, Y.; Yuan, Y.; Huang, J. *Nat. Photonics* **2015,** *9*, 679-687.

[29] Landi, G.; Neitzert, H. C.; Barone, C.; Mauro, C.; Lang, F.; Albrecht, S.; Rech, B.; Pagano, S. *Adv. Sci.* **2017,** 1700183.

[30] Fang, Y.; Huang, J. *Adv. Mater.* **2015,** *27*, 2804-2810.

[31] Cho, D.; Lee, H.; Shekhar, S.; Yang, M.; Park, J. Y.; Hong, S. *Sci. Rep.* **2017,** *7*, 43411.

[32] Kogan, S. *Electronic noise and fluctuations in solids*; Cambridge University Press: Cambridge, 1996.

[33] Lee, H.; Cho, D.; Shekhar, S.; Kim, J.; Park, J.; Hong, B. H.; Hong, S. *ACS Nano* **2016,** *10*, 10135-10142.

[34] Pisoni, A.; Jaćimović, J.; Barišić, O. S.; Spina, M.; Gaál, R.; Forró, L.; Horváth, E. *J. Phys. Chem. Lett.* **2014,** *5*, 2488-2492.

[35] Nakano, M.; Fukumura, T.; Toyosaki, H.; Ueno, K.; Kawasaki, M. *Jpn. J. Appl. Phys.* **2006,** *45*, L1061-L1063.

[36] Jayaraman, R.; Sodini, C. G. *IEEE Trans. Electron Devices* **1989,** *36*, 1773-1782.

[37] Celik-Butler, Z.; Hsiang, T. Y. *IEEE Trans. Electron Devices* **1988,** *35*, 1651-1655.

[38] Hooge, F. N.; Kleinpenning, T. G. M.; Vandamme, L. K. J. *Rep. Prog. Phys.* **1981,** *44*, 479-532.

[39] Zhao, T.; Shi, W.; Xi, J.; Wang, D.; Shuai, Z. *Sci. Rep.* **2016,** *6*, 19968.

[40] Bischak, C. G.; Sanehira, E. M.; Precht, J. T.; Luther, J. M.; Ginsberg, N. S. *Nano Lett.* **2015,** *15*, 4799-4807.

[41] Chen, H.-W.; Sakai, N.; Jena, A. K.; Sanehira, Y.; Ikegami, M.; Ho, K.-C.; Miyasaka, T. *J. Phys. Chem. Lett.* **2015,** *6*, 1773−1779.

[42] Gonzalez, R. C.; Woods, R. E. *Digital image processing*; Addison-Wesley: New York, 1992.

[43] deQuilettes, D. W.; Vorpahl, S. M.; Stranks, S. D.; Nagaoka, H.; Eperon, G. E.; Ziffer, M. E.; Snaith, H. J.; Ginger, D. S. *Science* **2015,** *348*, .683-686.

[44] Pecchia, A.; Gentilini, D.; Rossi, D.; derMaur, M. A.; Carlo, A. D. *Nano Lett.* **2016,** *16*, 988-992.

[45] Mandoc, M. M.; Kooistra, F. B.; Hummelen, J. C.; deBoer, B.; Blom, P. W. M. *Appl. Phys. Lett.* **2007,** *91*, 263505.

[46] Dimitropoulos, D.; Jhaveri, R.; Claps, R.; Woo, J. C. S.; Jalali, B. *Appl. Phys. Lett.* **2005,** *86*, 071115.

[47] Cowan, S. R.; Leong, W. L.; Banerji, N.; Dennler, G.; Heeger, A. J. *Adv. Funct. Mater.* **2011,** *21*, 3083-3092.

[48] Shao, Y.; Fang, Y.; Li, T.; Wang, Q.; Dong, Q.; Deng, Y.; Yuan, Y.; Wei, H.; Wang, M.; Gruverman, A.; Shield, J.; Huang, J. *Energy Environ. Sci.* **2016,** *9*, 1752-1759.

[49] Crandall, R. S. *J. Appl. Phys.* **1983,** *54*, 7176-7186.

[50] Lee, Y. S.; Gershon, T.; Gunawan, O.; Todorov, T. K.; Gokmen, T.; Virgus, Y.; Guha, S. *Adv. Energy Mater.* **2015,** *5*, 1401372.

[51] Bandić, Z. Z.; Bridger, P. M.; Piquette, E. C.; McGill, T. C. *Appl. Phys. Lett.* **1998,** *73*, 3276.

Chapter 3

Noise Scaling Behaviors in Molecular Junctions

3.1 Introduction

The basic research about molecular wires can provide fundamental understandings about charge transports in nanoscale materials and even allow one to envision advanced electronic devices based on a single molecular wire [1-11]. Many pioneering works reported studies on molecular wires, using methods based on various electrode-molecular wire junctions such as scanning probe-based junctions [2,7], mechanically-controllable break junctions [3,6], and sandwich junctions [1,3]. These methods allowed one to study various properties of molecular wires such as electrical conductivity, gate-voltage dependency of the conductivity, noise properties, and photo reactivity, which provided valuable insights about charge transports in molecular wires [1-3]. Especially, electrical noises in molecular wire junctions have been drawing increasing attentions because they can be an important parameter determining the performance of molecular wire-based devices and provide a clue to understand various aspects of molecular wires such as charge transport mechanisms [12], localized electronic states (or defects) in molecular tunnel barriers [13] and the coupling of molecular wires with metal electrodes [12,14]. However, there is a wide spectrum of factors affecting the electrical characteristics of such molecular wire

junctions, resulting in the large device-to-device variations of molecular wire junctions [15,16]. For example, previous reports showed that, even for the molecular wire junctions based on the same molecular wires, current and noise levels could vary over a few orders of magnitude, depending on devices [16]. Due to such variation and inconsistencies of measured results, it is often very difficult to identify the effect by molecular wires in the measured noise data [15]. Thus, the studies about electrical noises in molecular wires often required very difficult and time-consuming tasks such as thousands of device fabrications and repeated measurements to obtain statistically-meaningful data, which has been one of the major hurdles in the studies on the electrical noise sources in molecular wires [16].

In this dissertation, we report a strategy to directly map and identify the sources of electrical noises in the self-assembled monolayers of molecular wires. In this strategy, the maps of *electrical currents* and *frequency (f) spectra of noise power spectral densities (PSDs)* were measured on the patterns of different molecular wire layers via a scanning noise microscopy method [17] and utilized to analyze *electrical resistance values* and *noise sources* in the molecular wires, respectively. The frequency spectra of noise PSD measured from molecular wire junctions, regardless of molecular species, exhibited a characteristic $1/f^2$

behavior unlike a common *1/f* behavior of simple metal-metal nano-junctions, which was utilized to identify electrical signals originated from molecular wires. By mapping noise PSDs on the patterns of multiple molecular wires on a single substrate using a single probe, we could reliably compare the characteristics of noise sources in different molecular wires. Importantly, we could directly map the mean-square fluctuations of individual molecular resistances, which are responsible for the current noises in molecular wire junctions, on the layers of different molecular wires. The detailed analysis results showed that the mean-square fluctuations of the molecular resistance were linearly proportional to squared molecular resistances, implying that the noises in molecular wire junctions were mainly originated from the fluctuations of molecular wire-metal bondings. Furthermore, we could quantitatively map the frequency of such bond fluctuations on different molecular wire-metal junctions. The results showed that molecular wires with herringbone structures had more frequent bond fluctuations than linear molecular wires, which was attributed to the rather loose packing density of molecules with herringbone structures on gold surfaces. Since our strategy allows one to easily identify and reliably analyze electrical currents and noise sources in molecular wire junctions, it can be a major breakthrough, and it provides a simple but powerful tool for the research

about electronic systems based on molecular wires.

3.2 Experimental Setup

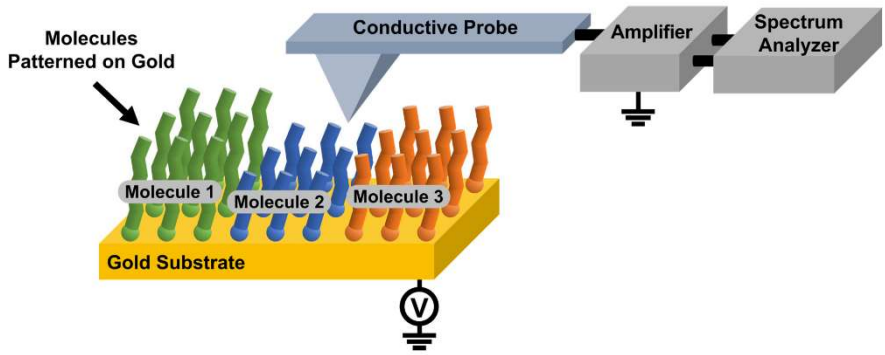

Figure 3-1 Schematic diagram depicting the experimental set-up for the measurement of electrical currents and noises in patterned layers of molecular wires. A Pt-based conducting probe installed on an AFM was placed on the patterns of molecular wire layers, and a bias voltage was applied between the probe and the underlying gold substrate. The contact force between the probe and molecular wires could be maintained as 1 μN using a force feedback loop in the AFM system. Electrical currents and noise PSDs of the currents were simultaneously measured using a preamplifier and a homemade spectrum analyzer. By scanning the probe above the patterned surface, the maps of electrical currents and noise PSDs could be obtained.

Figure 3-1 shows the schematic illustration of our experimental setup for the noise and current measurements on a patterned layer of molecular wires. In brief, we prepared the self-assembled monolayer (SAM) patterns of different molecular wires on a gold substrate via a micro-

contact printing method [18]. Then, a Pt-based conducting probe installed on a contact mode atomic force microscopy (AFM) system was approached to the sample with an AFM force feedback on, forming a metal/molecular wire/metal junction. In the contact mode operation, the contact force between the probe and the sample could be maintained as 1 μN using the contact force feedback loop in the AFM system. For the mapping of electrical currents and noises, a bias voltage was applied between the probe and the underlying gold substrate with the force feedback, and electrical currents through the gold/molecular wire/Pt probe junction were measured. The measured currents were converted to amplified voltage signals by a preamplifier (SR570, Stanford Research Systems). Subsequently, the noise PSD of the signals in a specific frequency range was measured utilizing a homemade spectrum analyzer. By scanning the probe on the molecular wire patterns during the measurement, the two-dimensional maps of currents and noise PSDs could be obtained. A typical scan speed was ~ 0.5 μm/s. Then, the measured *current* and *PSD* maps were analyzed to obtain the maps of *resistances* and *the mean-square fluctuations of resistances* of the patterned molecular wires, respectively. Note that the characteristics of scanning probe-based molecular junctions could vary due to the variations of used probes and substrates. However, in our strategy, we

could measure the noise characteristics of different molecular wires using a single measurement probe on the same substrate. Thus, the possible variation of molecular junctions, which has often been a serious problem in previous works, could be minimized, enabling reliable comparative studies of different molecular wires.

3.3 Characteristic Scaling Behavior of Current Noises in Molecular wire-Metal Probe Junctions

Figure 3-2*a* and *b* in the next page show the images of the *AFM topography* and the *electrical current map* measured on 1-nonanethiol (C9) SAM patterns on a gold substrate. The bias voltage of ~ 5 mV was applied between the gold substrate and the conducting AFM probe. The widths of the *C9* and the *gold* regions were ~ *4* μm and ~ *8* μm, respectively. The measured height of the C9 monolayer was about ~1.1 nm, which is consistent with the reported length of a C9 molecule [19]. The topography and current images show no bumps or cracks, indicating the high quality SAM of C9 molecules. It also should be noted that any mechanical or chemical distortion on the probe during

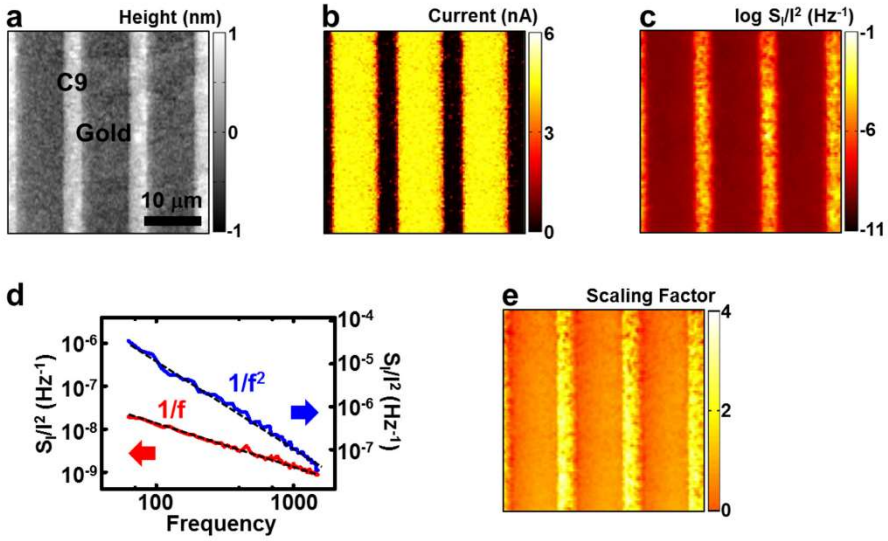

Figure 3-2 Characteristic scaling behavior of current noises in molecular wire-metal probe junctions. (a) AFM topography image showing line-shaped patterns of 1-nonanethiol (C9) SAM on a gold substrate. (b) Current map of the SAM patterns. (c) Current-normalized noise PSD map of the SAM patterns. (d) Graph showing noise PSD versus frequency data measured in a gold (red) and a molecular wire layer (blue) region on the sample. The data could be fitted by a $1/f^{\beta}$ curve with different values of the scaling factor β. The noise PSD spectra from a molecular wire region could be fitted by a $1/f^{2}$ curve corresponding to the scaling factor of ~2.0, while those from the gold region exhibited a typical *1/f* behavior with a scaling factor of ~1.0. (e) Scaling factor map of the noise PSD spectra measured on the SAM patterns. The *molecular wire* and *gold* regions exhibited the scaling factors of ~ *2.0* and ~ *1.0*, respectively.

the scanning could result in abrupt changes or distortions in the images. In such cases, the data were discarded, and the probe was replaced with a clean one. We could repeatedly image a specific region of a molecular

pattern by more than 5 times without abrupt changes or distortions in the imaging results. It indicates the distortion on the probe or samples during the scanning was minimal, and, at least in a presented image, we performed the noise measurement with the same probe condition. The electrical current level on molecular wire regions was ~ 100 times lower than that on Au regions, implying most of voltage drops occurred at the molecular wire junctions in our measurement system.

Our system allowed us to obtain the map of current-normalized noise PSD (S_I/I^2) (at 31.6 Hz) simultaneously while obtaining the topography and the current map (Figure 3-2c). Note that the noise level on the molecular wire (~ 10^{-5} Hz^{-1}) was much higher than that on the bare gold region (~ 10^{-9} Hz^{-1}). The low noise level in the gold region indicates negligible background noises in our AFM system with the contact force feedback on. On the other hand, the high noise level in the C9 monolayer region implies that the C9 molecular wires between the gold and the AFM probe were generating a significant amount of electrical noises.

In our set-up, we could place a conducting probe at a fixed location on the molecule-patterned sample and measure noise spectra from that location. Figure 3-2d shows current-normalized noise PSD spectra which were measured at two different regions: (i) a bare gold region (red line) and (ii) a C9 SAM region (blue line). In both cases,

noise PSD values were quite high at low-frequency conditions, and exponentially decreased with the increasing frequency, indicating the existence of frequency-dependent noise sources other than the frequency-independent Johnson–Nyquist noise sources in the sample. We fitted the noise PSD spectra using a function of a frequency f like $PSD = A/f^{\beta}$, where A and β were fitting parameters. The fitting curves are marked by black dashed lines in the Figure 3-2d. Here, the fitting parameter β gives useful information about how fast the noise PSD decreased with the increasing frequency, and it was named as "scaling factor". As indicated by the fitting curve (dashed line), the PSD measured at the gold region showed a typical *1/f* noise behavior with $\beta \sim 1$. On the other hand, when we measured noise spectra in the C9 region, a $1/f^2$ noise behavior with $\beta \sim 2$ was observed.

Previous works showed that a single noise source in an electrical channel can generate a current fluctuation with its own characteristic time τ [15]. And, the PSD spectra of noises generated from the noise source should have the form of Lorentzian [20]

(1) $$PSD \propto \frac{1}{1+(2\pi f\tau)^2}$$

At a rather high frequency condition of $2\pi f\tau >> 1$, the PSD can be approximated to be proportional to $\sim 1/f^2$ [13,15]. However, if a current

channel has a *large number of noise sources with different characteristic times*, the PSDs of the different noise sources are averaged out resulting in noise spectra proportional to *1/f* [15]. Thus, the observed 1/*f* behavior of the electrical noises in the gold film regions indicates *different* noise sources in gold films as well as the Pt probe. On the other hand, the noise spectra from C9 monolayers exhibited a $1/f^2$ behavior, indicating that the noises were mainly generated by the *uniform* noise sources in the molecular wire layer [13]. The measured PSD on the C9 monolayer was fitted by the Lorentzian curve, allowing us to estimate the time constant τ as 11 ms. It is consistent with a previously-reported value [13]. This characteristic feature of noises from molecular wire junctions could be utilized as a means to qualitatively distinguish the noises of *molecular wire junctions* from that of other *metallic junctions*.

We could measure the scaling factor β at each point on the C9 patterns to obtain a scaling factor map (Figure 3-2e). Here, the noise PSD was measured in the frequency range of 5.47 ~ 173 Hz at each point of the surface and utilized to estimate the scaling factors. Note that the scaling factor map shows a clear contrast between the molecular region ($\beta \sim 2.0$) and the gold region ($\beta \sim 1.0$). It should be mentioned that we could obtain the same consistent results from all different molecular wire

samples presented in this dissertation, indicating that this scaling analysis of noise spectra can be a simple but powerful means to identify the noises generated by molecular wires.

3.4 Mapping of Mean-Square Fluctuations of Molecular Resistances on SAM Patterns Comprised of Multiple Molecular Species

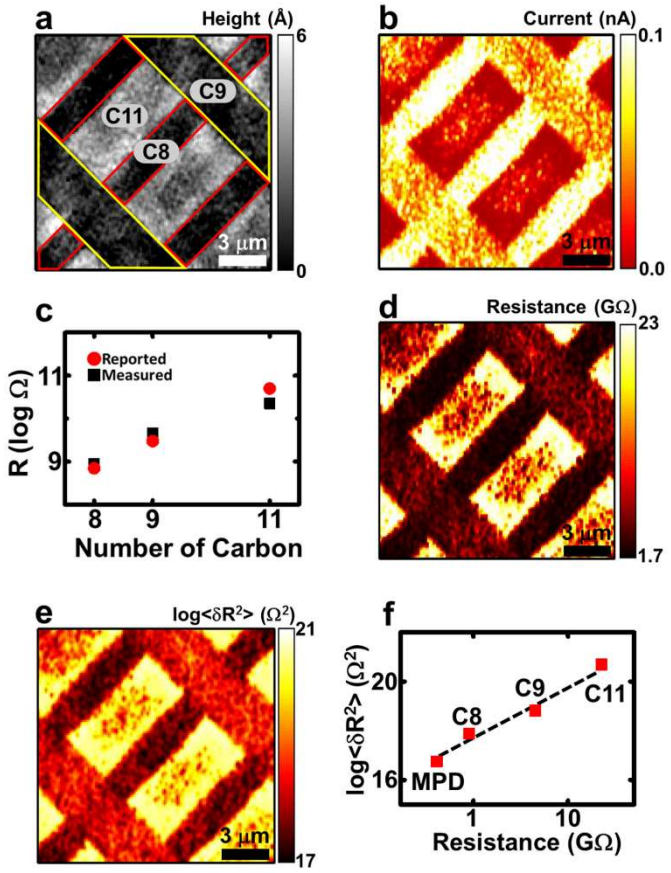

Figure 3-3 Mapping of the mean-square fluctuations of molecular resistances $<\delta R^2>$ on SAM patterns comprised of three different molecular wires with different lengths on a gold substrate: 1-octanethiol (C8), 1-nonanethiol (C9), and 1-undecanethiol (C11). (a) AFM topography image. The areas surrounded by *red* and *yellow* lines were coated with the SAMs of *C8* and *C9* molecular wires, respectively. The other regions were covered with C11 SAMs. (b) Current map. The bias voltage of 5 mV was applied between the probe and the

gold substrate. (c) Reported (red circles) and measured (black squares) resistance values of individual C8, C9, C11 molecules. (d) Map showing the resistance of individual molecular wires in the SAM patterns. (e) Map showing the mean-square fluctuations of molecular resistances $<\delta R^2>$ obtained from the PSD and current images. Importantly, we could quantitatively compare $<\delta R^2>$ values of different molecular wires using the map. (f) $<\delta R^2>$ versus molecular resistance graph. The $<\delta R^2>$ was proportional to the squared molecular resistance R^2.

Figure 3-3*a* and *b* show the *topography* and *current* images of a molecular pattern comprised of three different thiol molecular species with different chain lengths: 1-octanethiol, 1-nonanethiol, and 1-undecanethiol (C8, C9, and C11). Briefly, C9 SAMs were first patterned on a gold substrate via the micro-contact printing method (regions in yellow trapezoids). Then, C8 SAMs (regions surrounded by red lines) were patterned in a perpendicular direction to the C9 SAMs. Finally, the patterned substrate was dipped in a 0.2 mM solution of C11 molecules so that the C11 molecules filled up the remaining bare gold region. The topography image shows that C11 SAMs were higher than other SAMs about ~ 0.4 nm, and the averaged height difference between C8 and C9 SAMs was ~ 0.1 nm, which is consistent with the previously-reported results [16]. The current map shows clear differences of current levels between C8, C9 and C11 regions. A molecular wire with a longer chain

length exhibited a lower current level compared with a shorter molecular wire. Previous reports showed that tunnel-currents through molecular wire SAMs decreased exponentially with increasing molecular lengths and, thus, current levels were extremely sensitive to molecular lengths, which is also consistent with our results [16,21,22].

When a conducting probe with its contact area of A and a known bias voltage (V) was utilized to measure electrical currents (I) through a layer of molecular wires, the resistance (R) of a single molecular wire in the layer can be written like

$$R = A\,(nV / I) \tag{2}$$

where n represents *the number of molecules in the unit area of the molecular wire layer*. In the case of alkanethiol monolayers, the n is reported as ~ 4.65 molecules/nm^2 [23]. Here, the contact area A of the conducting probe is still an unknown parameter. However, it also should be noted that since we utilized the same probe to measure electrical currents from different molecular wires (Figure 3-3b), the values of A for the measurements on different molecular wires were the same, and we could estimate the value of A by utilizing it as a fitting parameter. The red circular dots in Figure 3-3c show the reported values of a single molecular resistance R of C8, C9, and C11 molecular wires [24]. Utilizing the Eq. (2) with A as a single fitting parameter, the reported

resistance values could be fitted very well from our measured data (black square dots in Figure 3-3c). The contact area A estimated through the fitting was ~ 9.6 nm^2, which is also consistent with the dimension of our conducting probe [25].

Using the current map in Figure 3-3b and the estimated contact area A, we could obtain the map of the single-molecule resistances in the different molecular layers (Figure 3-3d). The single-molecule resistance values of *C8*, *C9* and *C11* molecules were ~ *0.9*, *4.5* and *22.5 GΩ*, respectively. It also should be mentioned that the scaling factor β of the noise-frequency spectra measured on these different molecular wire regions exhibited a value close to ~2.0, indicating that we are measuring the currents and resistances originated from molecular wires rather than metal-metal nanocontacts. In our experiment, since a single probe was utilized to measure resistance values of different molecular wires under the same conditions, the possible variation of molecular wire junctions can be minimized and we can precisely estimate the ratio of molecular resistance values of different molecular wires in Figure 3-3d.

The electrical noise generated in molecular wire junctions is an important parameter which should determine the performance of molecular wire-based devices. In addition to electrical currents, we could also measure the map of electrical current noises on the layers of

different molecular wires. Further, here, we propose a theoretical model to quantitatively estimate the mean-square fluctuations of single-molecule resistances of molecular wires. Consider a molecular wire whose resistance exhibits fluctuations with a characteristic time τ. The PSD (S_R) of the resistance fluctuation of the molecular wire, at a frequency f, can be written as [26],

(3) $$S_R(f) = 2\langle \delta R^2 \rangle \cdot \frac{1}{\pi f_0} \cdot \frac{1}{1+(f/f_0)^2}$$

Here, $<\delta R^2>$ and f_0 are *the mean-square fluctuations of molecular resistance* and $1/(2\pi\tau)$, respectively. Previous studies showed that electrons tunnel through a molecular junction can give some energy to the junction by interacting with phonons [20]. Further, it was suggested that the energy from the tunneling carriers is the main source of the energy needed for the resistance fluctuation of a molecular junction, and thus the rate of the fluctuations should be proportional to the amount of currents through the junction [20,26]. Thus, with a constant B, f_0 can be written as [26],

(4) $$f_0 = BI$$

Here, I denotes the current through a molecular wire. Utilizing the Eq. (4) and the measured values of f_0 and I, we could obtain the constant B

as ~ 1.3x10^4 Hz/nA. At a high frequency condition of f/f_0>>1, the Eq. (3) can be rewritten like,

(5) $$S_R(f) = \frac{2}{\pi}\langle \delta R^2 \rangle \cdot \frac{BI}{f^2}$$

The noise PSD values of the fluctuations in the *resistance* and *current* are related like [27]

(6) $$\frac{S_I(f)}{I^2} = \frac{S_R(f)}{R^2}$$

And, from the Eq. (5), $<\delta R^2>$ can be written as,

(7) $$\langle \delta R^2 \rangle = \frac{\pi}{2} \cdot \frac{f^2 R^2}{BI} \cdot \frac{S_I(f)}{I^2}$$

Figure 3-3e shows the map of $<\delta R^2>$ obtained utilizing the Eq. (7). The S_I/I^2 map measured with the Figure 3-3a and b was utilized for the calculation. The $<\delta R^2>$ map shows the clear differences of $<\delta R^2>$ levels for different molecular wires. The $<\delta R^2>$ in the *C8*, *C9* and *C11* regions were ~ $7.6x10^{17}$, $6.7x10^{18}$ and $4.8x10^{20}$ Ω^2, respectively. Significantly, we could, for the first time, quantitatively measure and compare the mean-square fluctuations of molecular resistances of different molecular wires, which should be a significant breakthrough in noise researches on molecular wires.

Figure 3-3f shows the $<\delta R^2>$ values as a function of a molecular resistance *R*. Here, the $<\delta R^2>$ value of 4-mercaptopyridine (MPD)

molecule was estimated from the S/I^2 map measured on a MPD/C9 patterned sample. As indicated by a dashed line, the $<\delta R^2>$ was found to be proportional to the squared molecular resistance (R^2) like

(8) $$<\delta R^2> \sim 0.50 \text{ x } R^2$$

Significantly, although the MPD and other alkanethiol molecules had completely different molecular chains with different lengths and molecular structures, they still exhibited a similar behavior. Previous works showed that the resistance of an insulating molecular wire with its length d can be written like [28],

(9) $$R = R_0 \exp(\alpha \cdot d)$$

Here, R_0 corresponds to the contact resistance which should depend on the metal-molecule bonding and the contact between the molecule and the AFM probe [28]. Since we utilized the same probe and molecules with the same thiol bonding, the contact resistance R_0 should be almost identical for all molecular wires in the graph [28]. α is the tunneling attenuation factor which depends only on the chain of the molecular wires [28]. From the Eq. (9), the mean square fluctuation $<\delta R^2>$ of the molecular resistance, which is responsible for the current noises in molecular wire junctions, can be written like,

(10) $$\langle \delta R^2 \rangle = \left(\frac{\langle \delta {R_0}^2 \rangle}{R_0^2} + d^2 \cdot \langle \delta \alpha^2 \rangle + \alpha^2 \cdot \langle \delta d^2 \rangle \right) \cdot R^2$$

Here, the first term is originated from the molecular contact resistance and its fluctuation [29,30]. In our case, since we utilized the same AFM probe and molecules with the same *thiol* bondings, the first term should be almost constant for all molecular species in Figure 3-3f. On the other hand, the second and the third terms came from the properties of molecular chains and their fluctuations such as a molecular length fluctuation and chain twisting [31]. Since the conjugated MPD and other alkanethiol molecules in our experiment had quite different molecular chains, these terms should vary significantly depending on molecular species. However, our results show that $\langle \delta R^2 \rangle \propto R^2$ though our molecular species had quite different chains. It indicates that the electrical noise of molecular wire junctions in our experiments was mainly originated from the fluctuation of the metal-molecular wire bonding. Although extensive efforts have been given to understand the charge transport and noises in molecular wire junctions, it is still uncertain about what is the dominant noise source in the molecular wire junctions [20]. Our results imply that electrical noises in molecular wire junctions are mainly originated from the fluctuation of molecular bonds, which can be a valuable insight about the transport phenomena in molecular wire-based devices.

3.5 Mapping of Noise Spectral Characteristics on SAM Patterns Comprised of Molecular Wires with Different Chain Structures

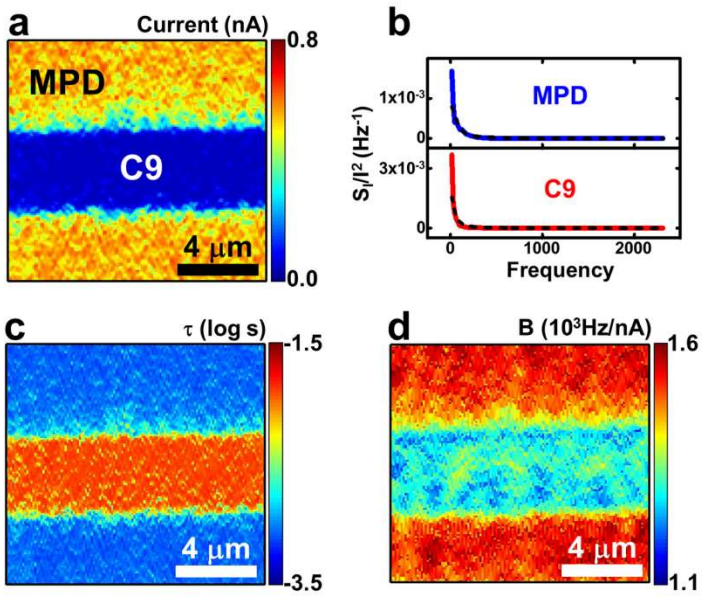

Figure 3-4 Noise spectral characteristics of MPD and C9 molecules. (a) Current map measured on the patterns of MPD (yellow region) and C9 (blue region) molecules. (b) Current-normalized PSD spectra of MPD (blue lines) and C9 (red lines) molecules and their Lorentzian fittings (black dashed lines). (c) Map of τ measured on the patterns of MPD (blue region) and C9 (orange regions) molecules. The MPD regions exhibited shorter τ values (~ 0.9 ms) compared to the C9 regions (~ 12 ms), indicating more frequent bond fluctuations on the MPD molecular junctions. (d) Map of the proportional factor B measured on the patterns of MPD (red or yellow regions) and C9 (blue or emerald region) molecules. The MPD region exhibited higher B than the C9 region, implying that the bond-fluctuation events with the same currents can occur more frequently in the MPD molecules compared to the C9 molecules.

The spectral analyses of a noise spectrum can be utilized to reveal more detailed nature of molecular wire-based junctions (Figure 3-4). Figure 3-4a shows the current map taken on the patterns of the conjugated MPD and alkane chain-based C9 molecules. Since the MPD molecule has conjugated backbones of herringbone structures and a shorter chain length than the C9 molecule, the current level on the MPD regions appeared to be much higher than that on the C9 regions. Figure 3-4b shows current-normalized PSD (S_I/I^2) spectra which were measured in a MPD region (blue line) and a C9 region (red line). Both regions exhibited $1/f^2$ noise characteristics. The PSD spectra on *MPD* and *C9* regions could be fitted well using Lorentzian curves (black dashed lines) with fitting parameters τ of $\sim$ *1.3 ms* and *11.5 ms*, respectively. The results are compatible with the previously reported values [13,26]. Here, the fitting parameter τ is the characteristic time which should be proportional to the mean time interval between each bond-fluctuation event. Thus, the shorter τ of the MPD molecule indicates that the bond-fluctuation events occurred more frequently in the MPD molecule than the C9 molecule. One plausible explanation can be the larger currents on the MPD molecular regions because the energy needed for the bond fluctuation is mostly provided by currents passing through molecular junctions [20,26].

Furthermore, the relatively low packing density and rather high defect densities of MPD molecular layers may have contributed to more frequent bond fluctuations [20].

For more detailed analysis, we obtained the map of τ on the molecular layers (Figure 3-4c). By plugging the Eq. (4) and the fitting result of the Eq. (8) into the Eq. (7), the τ can be written as

(11) $$\tau = \frac{0.50}{\pi^2} \cdot \frac{1}{f^2} \cdot \left(\frac{S_I(f)}{I^2}\right)^{-1}$$

Utilizing above equation, we could calculate τ on each point of the MPD/C9 patterns to obtain a τ map (Figure 3-4c) from the PSD and current maps. The averaged τ on the *MPD* and *C9* regions was ~ *0.9* and *12* ms, respectively. The result is consistent with the observations which were obtained using the frequency spectra in the Figure 3-4b. The map shows that the molecular bonds in the MPD layers fluctuate more frequently than those in the C9 molecular layers. Note that our map whose resolution is 128 by 128 contains ten thousands of τ value data measured from molecular junctions using the same AFM probe. Therefore, the consistency of our results throughout the whole map should support the reliability and reproducibility of our analysis.

Since the fluctuations in molecular junctions are mainly triggered by the currents as described in the Eq. (4) [20,26], the τ can be written like

(12) $$\tau = 1/(2\pi f_0) = 1/(2\pi BI)$$

Here, the proportional factor *B* represents the frequency of molecular bond fluctuations with the same amount of currents, and, thus, it can be a very useful characteristic parameter showing the noise properties of specific molecular wires. Utilizing the τ map, the current map and the Eq. (12), we could estimate the map of *B* on the MPD/C9 patterns (Figure 3-4d). The averaged values of *B* on the *MPD* and *C9* regions were ~ $1.52x10^3$ and ~ $1.29x10^3$ Hz/nA, respectively. It indicates that, with the same amount of currents, the molecular bondings of MPD molecules fluctuate more frequently than those of *C9* molecules. Previously, it was suggested that the characteristic frequency of noises in molecular layers will depend on how densely the molecules cover the gold substrate [20]. For example, in case of a densely-packed molecular layer, the lateral motion of the Au–S bondings could be hindered and the number of bond-fluctuation events per unit-time should be reduced compared to a loosely-packed molecular layer [20,32]. It was also reported that the packing density of the MPD molecule with a pyridine ring is lower than

that of the C9 molecule [33]. Thus, the higher *B* of the *MPD* molecule in our data could be attributed to the lower packing density of the MPD molecules compared to the *C9* molecules. Our results show that we can expect more molecular bond fluctuations and thus electrical noises with a higher frequency on the MPD-based electrical junctions than C9-based ones. Note that the noise characteristics of molecular wires directly affect the quality of molecular wire junctions and eventually determine the performance of molecular wire-based devices. Our method allowed us to quantitatively evaluate the noise characteristics of molecular wire junctions, which should provide a useful guideline in developing molecule-based devices.

3.6 Summary

In summary, we have developed a strategy for the direct mapping and identification of noise sources in molecular wire layers. In the strategy, we patterned different molecules on the same gold substrate and placed a conductive AFM probe with a AFM force feedback on the pattern to measure electrical currents and the noise PSD at a specific frequency simultaneously. By scanning the probe above the molecular patterns during the measurement, the maps of *electrical currents* and *noise PSDs* were obtained and utilized for the comparative analysis of the *electrical*

resistance values and the *noise characteristic parameters* in different molecular wires, respectively. Importantly, we observed characteristic $1/f^2$ noise behaviors of noise PSDs measured from molecular wires, while a simple metallic junction exhibited a typical *1/f* noise behavior, which could be used as a means to qualitatively distinguish the electrical signals of molecular wire junctions from those of metallic junctions. In addition, we successfully patterned three different molecular wires on the same gold substrate and mapped the mean-square fluctuations of molecular resistances $<\delta R^2>$ on the molecular patterns. Interestingly, we found that the $<\delta R^2>$ was proportional to the squared molecular resistance R^2, implying that the noises in molecular wire junctions were mostly originated from the fluctuation of molecular wire-metal bondings. Furthermore, noise spectral analysis showed that the bond-fluctuation events could occur more frequently in a loosely-packed molecular layer than a densely-packed molecular layer. Presumably, the lateral motion of the metal-molecule bondings could be hindered in a densely packed environment, reducing the number of the bond fluctuation events per unit-time. Our results provide new insights about the electrical noises in molecular wires and allow one to characterize molecular wire devices systematically. Considering that it has been extremely difficult and time-consuming to measure the noise characteristics of molecular wires

reliably, our strategy can be a powerful tool and should be a significant breakthrough in noise studies on molecular wire-based devices.

3.7 References

[1] Kushmerick, J. G.; Holt, D. B.; Yang, J. C.; Naciri, J.; Moore, M. H.; Shashidhar, R. *Phys. Rev. Lett.* **2002,** *89*, 086802.

[2] Nitzan, A.; Ratner, M. A. *Science* **2003,** *300*, 1384-1389.

[3] Tao, N. J. *Nat.* Nanotechnol. **2006,** *1*, 173-181.

[4] Song, H.; Kim, Y.; Jang, Y. H.; Jeong, H.; Reed, M. A.; Lee, T. *Nature* **2009,** *462*, 1039-1043.

[5] Aradhya, S. V.; Venkataraman, L. *Nat. Nanotechnol.* **2013,** *8*, 399-410.

[6] Xiang, D.; Jeong, H.; Kim, D.; Lee, T.; Cheng, Y. J.; Wang, Q. L.; Mayer, D. *Nano Lett.* **2013,** *13*, 2809-2813.

[7] Xiang, D.; Jeong, H.; Lee, T.; Mayer, D. *Adv. Mater.* **2013,** *25*, 4845-4867.

[8] Kim, T.; Darancet, P.; Widawsky, J. R.; Kotiuga, M.; Quek, S. Y.; Neaton, J. B.; Venkataraman, L. *Nano Lett.* **2014,** *14*, 794-798.

[9] White, A. J.; Tretiak, S.; Galperin, M. *Nano Lett.* **2014,** *14*, 699-703.

[10] Su, T. A.; Li, H.; Steigerwald, M. L.; Venkataraman, L.; Nuckolls, C. *Nature Chem.* **2015,** *7*, 215-220.

[11] Li, H.; Su, T. A.; Zhang, V.; Steigerwald, M. L.; Nuckolls, C.; Venkataraman, L. *J. Am. Chem. Soc.* **2015,** *137*, 5028-5033.

[12] Clement, N.; Pleutin, S.; Seitz, O.; Lenfant, S.; Vuillaume, D. *Phys. Rev. B* **2007,** *76*, 205407.

[13] Kim, Y.; Song, H.; Kim, D.; Lee, T.; Jeong, H. *Acs Nano* **2010,** *4*, 4426-4430.

[14] Adak, O.; Rosenthal, E.; Meisner, J.; Andrade, E. F.; Pasupathy, A.

N.; Nuckolls, C.; Hybertsen, M. S.; Venkataraman, L. *Nano Lett.* **2015,** *15*, 4143-4149.

[15] Ochs, R.; Secker, D.; Elbing, M.; Mayor, M.; Weber, H. B. *Faraday Discuss.* **2006,** *131*, 281-289.

[16] Scaini, D.; Castronovo, M.; Casalis, L.; Scoles, G. *Acs Nano* **2008,** *2*, 507-515.

[17] Sung, M. G.; Lee, H.; Heo, K.; Byun, K.-E.; Kim, T.; Seo, D. H.; Seo, S.; Hong, S. *Acs Nano* **2011,** *5*, 8620-8628.

[18] Wilbur, J. L.; Kumar, A.; Kim, E.; Whitesides, G. M. *Adv. Mater.* **1994,** *6*, 600-604.

[19] Liu, G.-Y.; Xu, S.; Qian, Y. *Acc. Chem. Res.* **2000,** *33*, 457-466.

[20] Xiang, D.; Lee, T.; Kim, Y.; Mei, T.; Wang, Q. *Nanoscale* **2014,** *6*, 13396–13401.

[21] Wang, W. Y.; Lee, T.; Reed, M. A. *Phys Rev B* **2003,** *68*, 035416.

[22] Thuo, M. M.; Reus, W. F.; Nijhuis, C. A.; Barber, J. R.; Kim, C.; Schulz, M. D.; Whitesides, G. M. *J. Am. Chem. Soc.* **2011,** *133*, 2962-2975.

[23] Poirier, G. E.; Tarlov, M. J. *Langmuir* **1994,** *10*, 2853-2856.

[24] McCreery, R. L. *Chem. Mater.* **2004,** *16*, 4477-4496.

[25] Pérez-Madrigal, M. M.; Giannotti, M. I.; Armelin, E.; Sanz,F.; Alemán, C. *Polym. Chem.* **2014,** *5*, 1248−1257.

[26] Sydoruk, V. A.; Xiang, D.; Vitusevich, S. A.; Petrychuk, M. V.; Vladyka, A.; Zhang, Y.; Offenhausser, A.; Kochelap, V. A.; Belyaev, A. E.; Mayer, D. *J. Appl. Phys.* **2012,** *112*, 014908.

[27] Kogan, S. *Electronic noise and fluctuations in solids*; Cambridge University Press: Cambridge, 1996.

[28] Kim, B.; Beebe, J. M.; Jun, Y.; Zhu, X.-Y.; Frisbie, C. D. *J. Am.*

Chem. Soc. **2006,** *128*, 4970-4971.

[29] Ramachandran, G. K.; Hopson, T. J.; Rawlett, A. M.; Nagahara, L. A.; Primak, A.; Lindsay, S. M. *Science* **2003,** *300*, 1413-1416.

[30] Huang, Z.; Chen, F.; Bennett, P. A.; Tao, N. *J. Am. Chem. Soc.* **2007,** *129*, 13225–13231.

[31] Patrone, L.; Palacin, S.; Charlier, J.; Armand, F.; Bourgoin, J. P.; Tang, H.; Gauthier, S. *Phys. Rev. Lett.* **2003,** *91*, 096802.

[32] Donhauser, Z. J.; Mantooth, B. A.; Kelly, K. F.; Bumm, L. A.; Monnell, J. D.; Stapleton, J. J.; Price Jr., D. W.; Rawlett, A. M.; Allara, D. L.; Tour, J. M.; Weiss, P. S. *Science* **2001,** *292*, 2303-2307.

[33] Sawaguchi, T.; Mizutani, F.; Taniguchi, I. *Langmuir* **1998,** *14*, 3565-3569.

Chapter 4

Vibrational Noise Spectroscopy

4.1 Introduction

Experimental measurements about molecular vibrational modes of molecular species adsorbed on solid substrates provide versatile information about their molecular structures and often allow one to identify unknown molecular species [1]. Well-known workhorse techniques for such measurements include Raman spectroscopy [1] and inelastic electron tunneling spectroscopy (IETS) [2,3]. For some applications such as molecular electronics and nanomaterials analyses, it is important to map the distribution of adsorbed molecular species on solid substrates with a nanoscale resolution by measuring their vibrational modes [4]. In such cases, one could take advantage of the strategy combining the molecular vibrational spectroscopy techniques with scanning probe microscopy (SPM) methods such as a scanning tunneling microscopy (STM) [5] and an atomic force microscopy (AFM) [4]. For an example, STM probes have been used to perform nanoscale inelastic electron tunneling spectroscopy (IETS) measurements, enabling nanoscale mapping of molecular vibrational modes of organic molecules on solid substrates [6]. However, it usually requires cryogenic temperatures, restricting its application for samples at room temperature [7]. In addition, Raman spectroscopy has been combined with various SPMs to optically image molecular vibrational modes with nanoscale

resolutions at room temperature conditions [4,5]. However, an exquisite experimental setup with a highly-optimized SPM probe is required to build a reliable Raman-SPM system, making the measurements quite costly [8,9]. On the other hand, electrical noises, the temporal fluctuations of currents, in molecular junctions have been drawing attentions because the noises can provide versatile information that is often very difficult to obtain by other measurement methods [10-12]. Previous studies showed that molecular vibrational mode could be evaluated by statistically analyzing the fluctuations of multiple current (I)-bias voltage (V_b) spectra measured on a molecular junction [13,14]. However, it is often time-consuming to measure such multiple I-V_b data enough to obtain statistically meaningful results. In addition, such repetitive electrical measurements on a fixed location possibly cause damages on measured samples. Thus, the method has been very difficult to be used for the nanoscale imaging of molecular vibration modes.

Herein, we report a method to identify and map vibrational modes of molecular wires on a conducting solid substrate. In this method, a conducting probe installed on an AFM made a direct contact with molecular-wire layers on a conducting substrate and swept on the layer while measuring noise power spectral density (PSD). Then, the noise PSD data measured with different bias voltages were utilized to identify

the molecular vibrational modes stimulating the electrical noises. We found that an external bias voltage stimulated a specific molecular vibration mode, resulting in an enhanced electrical noise at the voltage. In this sense, the method is named here as “vibrational noise spectroscopy (VNS)”. Using the method, we could identify versatile molecular vibrational modes of molecular wires on Au substrates. Furthermore, we could map the distribution of vibrational modes on the patterns comprised of different molecular wires. Interestingly, we found that the strength of enhanced noise PSD under different bias voltages could be utilized to quantitatively estimate the densities of specific vibration modes in the layers of different molecular wires. Since our method allows one to map molecular vibrational modes under ambient conditions with a nanoscale resolution, it can be a simple but powerful tool for versatile basic researches and practical applications including molecular electronics and nanoscale material analyses in general.

4.2 Scanning Vibrational Noise Spectroscopy Setup

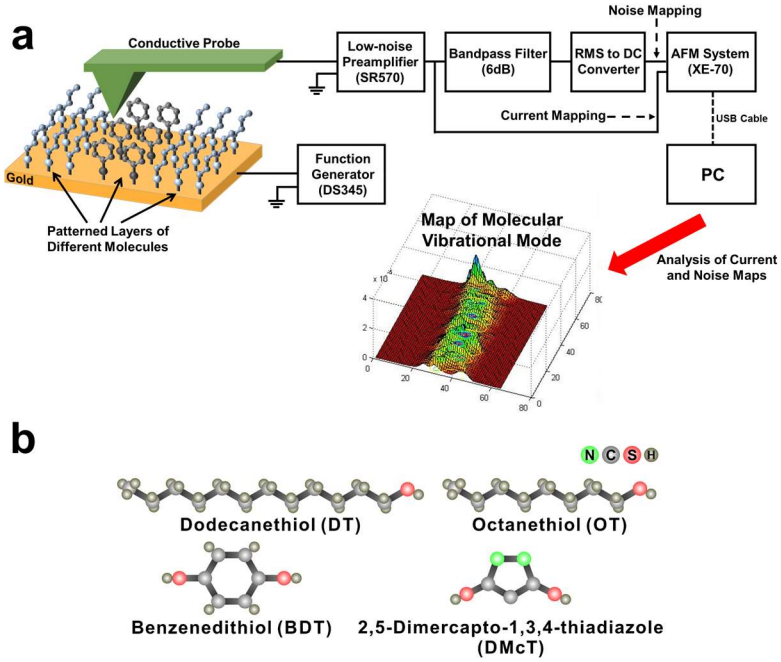

Figure 4-1 Schematic diagram depicting our scanning vibrational noise spectroscopy setup and the structures of molecular wires used in this work. (a) Schematic diagram showing our scanning vibrational noise spectroscopy setup. We combined a conducting AFM system with an electronic noise measurement system including a homemade spectrum analyzer, to measure current and noise maps on the patterns of molecular wires. The measured current and noise PSD values were analyzed to map the distribution of molecular vibrational modes. (b) Structures of molecules used in this work.

The schematic diagram in Figure 4-1a shows our setup for the noise and current measurements for the patterned layers of molecular wires on a gold substrate. For a noise spectroscopy experiment, a Pt-based conducting probe (25Pt300B from Park Systems, spring constant ~18

N/m) installed on an AFM system (XE-70, Park System) was placed on a molecular-wire sample to form a metal/molecule/metal junction. The contact force of the probe was maintained as 1 μN via a contact force feedback loop in the AFM system. For the mapping of electrical currents and noises, a DC bias voltage was applied between the gold substrate and the Pt probe by using a function generator (DS345, Stanford Research Systems). The electrical currents through the gold/molecule/Pt probe were measured and converted to amplified voltage signals by using a low-noise preamplifier (SR570, Stanford Research Systems). Simultaneously, electrical noises, the fluctuating components of the current signals, were collected using a band-pass filter (6 dB) in the SR570 preamplifier, and the RMS power of the collected noises was obtained by a homemade RMS-to-DC converter built using an AD737 chip (purchased from Analog Devices) [15]. By dividing the square of the measured RMS noise power with the bandwidth of the band-pass filter, we obtained the absolute current-noise PSD value (S_I) at the central frequency of the band-pass filter. The current and noise PSD values measured at a specific location on the molecular layers were recorded. By scanning the AFM probe on the molecular patterns during the measurement, the two-dimensional maps of currents and noise PSDs could be obtained. The measured current and noise PSD maps were

analyzed to obtain the map showing the distribution of molecular vibrational modes on the molecular layer. Note that our noise PSD measurements are based on the frequency-domain measurement of currents using a band-pass filter and a RMS to DC converter. This enabled the real-time measurements of the noise PSD value at a frequency (f), enabling the fast high-resolution imaging of electrical noises on molecular wire layers.

Figure 4-1b shows the structures of molecules used in our experiments. We used a set of alkanethiol molecules with different alkyl chain lengths, namely, dodecanethiol (DT) and octanethiol (OT). In addition, the benzenedithiol (BDT) and 2,5-dimercapto-1,3,4-thiadiazole (DMcT) molecules were studied. All the molecules bind on a gold substrate by forming S-Au bonds.

4.3 Spectral Characteristics of Noises Measured on a Molecule-Patterned Gold Substrate

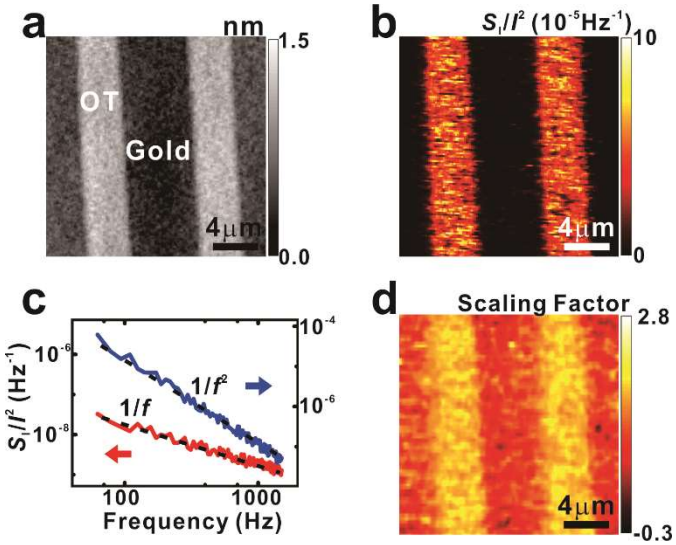

Figure 4-2 Identification of electrical noises from the junctions of molecular wires via frequency spectra. (a) AFM topography image showing line-shaped patterns of OT molecules on a gold substrate. (b) Current-normalized noise PSD map on the OT pattern. (c) Graph showing current-normalized noise PSD versus frequency spectra measured on the regions of a bare gold surface (red) and OT molecular layers (blue). The spectra could be fitted by a $1/f^{\beta}$ curve to obtain the values of the scaling factor β. The noise PSD spectra from a molecular region could be fitted by a $1/f^2$ curve corresponding to the scaling factor of ~2.0, while those from the gold region exhibited a typical $1/f$ behavior with a scaling factor of ~1.0. (d) Map of the scaling factor β estimated from the noise PSD measurements at different frequencies. The regions of *OT molecules* and *gold* exhibited the scaling factor β of *~2.0* and *~1.0*, respectively.

Figure 4-2a shows an AFM topography image measured on the self-assembled monolayers (SAMs) of OT molecules patterned on a gold

substrate. The widths of the *OT* and the *gold* regions were *~4* μm and *~6* μm, respectively. The measured height of the OT monolayer was about ~1.1 nm, which is consistent with the previously-reported length of OT [16]. The topography image shows the uniform layers of OT without any serious defects on the layers. In addition, it should be mentioned that when the conducting AFM probe was damaged during the measurement, the topography images were easily distorted. Thus, the clean topography image without sudden fluctuations indicates that the conducting probe did not change and it made a stable electrical contact with the molecular wire layer during the measurement.

We could measure the map of current-normalized noise PSD (S_I/I^2) (at 173 Hz) while simultaneously obtaining the topography (Figure 4-2b). The bias voltage of a 5 mV was applied between the gold substrate and the conducting probe. Note that the noise level on the OT molecules (~10^{-5} Hz^{-1}) was much higher than that on the bare gold region (~10^{-8} Hz^{-1}). The low noise level in the gold region indicates rather small background noises in our system. On the other hand, the high noise level in the OT molecular region implies that the OT molecules between the gold and the conducting probe were the major source of electrical noises. In this case, we could assume that the most of the noises originated in

the fluctuation in the molecule parts and analyze the noise data to obtain the information about the molecular wires.

We could place the conducting AFM probe at a specific location on the molecule layer and measure frequency-dependent noise PSD spectra from that location. Figure 4-2c shows current-normalized noise PSD spectra which were measured at a bare gold region (red line) and an OT molecule region (blue line). In both cases, noise PSDs were quite high at a low-frequency condition and rapidly decreased with an increasing frequency, showing the existence of strong frequency-dependent noises. We fitted the noise PSD spectra to the function of A/f^{β} to estimate the scaling factor β, where A is a constant fitting parameter. Note that the PSD measured at the gold region showed a typical *1/f* noise behavior ($\beta \sim 1$). However, when we measured noise spectra in the OT molecule region, a $1/f^2$ noise behavior ($\beta \sim 2$) was observed. Such a $1/f^2$ noise behavior has been reported as a typical behavior for nanoscale molecular junctions where most of electrical noises were generated by a small number of noise sources [17]. In our works, this characteristic feature of noise PSDs from molecular wires was utilized as a means to qualitatively distinguish the noises of molecules from that of bare Au surfaces [17].

We could measure the scaling factor β on each point on the OT pattern and obtain a scaling factor map (Figure 4-2d). Here, the noise PSD values were measured in the frequency range of 5.47 ~ 173 Hz at each point of the surface and utilized to estimate the scaling factors. Note that the scaling factor map shows a strong contrast between the OT region ($\beta \sim$ 2.0) and the gold region ($\beta \sim$ 1.0). We could consistently obtain the scaling parameter ~ 2 from all molecular wires in this study, supporting that measured noise signals in molecules were from the molecule parts rather than other conducting parts in our measurement setup.

4.4 Identification of Molecular Vibrational Modes Using Bias Dependence of Current Noises

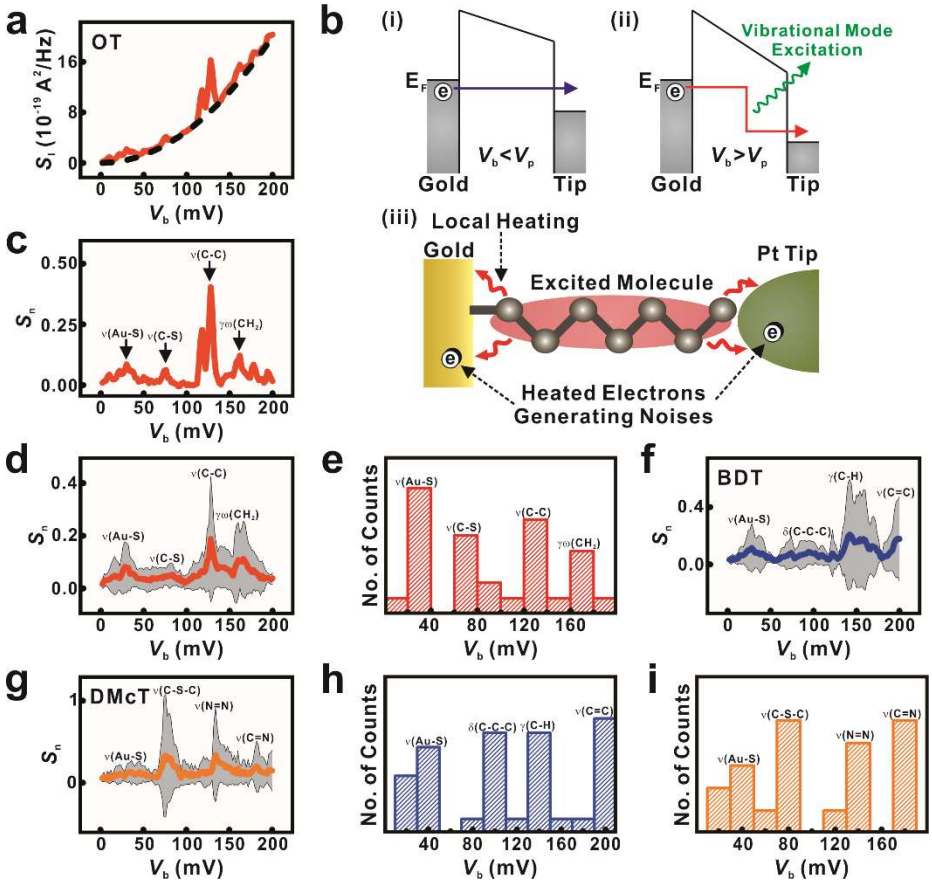

Figure 4-3 Identification of molecular vibrational modes using voltage-dependent noise PSD spectra. (a) S_I (at 95 Hz) versus V_b graph measured on OT molecules. By subtracting noise component proportional to the V_b^2 (black dashed line) from the S_I, we could obtain the $S_{I,\text{local heating}}$ from molecular vibrational modes. (b) Schematic diagram showing the electron tunneling (i, ii) and noise generation processes via local heating (iii) in a molecular junction. When the inelastic tunneling occurs at the junction, electrons near the junction are locally heated and the enhanced kinetic motions of the electrons induce additional electrical noises. (c) S_n versus V_b plot calculated from the Figure 4-

3a with V_0 = 200 mV. The distribution of peaks in the graph agreed well with reported molecular vibrational modes of the OT. (d) Graph showing the average of the S_n graphs measured at different positions on the OT layer. The averaged S_n also has peaks at the vibrational mode energies of the OT. (e) Histogram showing the distribution of peaks in S_n graphs from the OT. The peaks were frequently observed near the vibrational mode energies. (*f*,*g*) Averaged S_n graph on a *BDT* and *DMcT* layers, respectively. Vibrational modes assigned to the observed peaks were indicated. (*h*,*i*) Histograms showing the distribution of peaks in S_n graphs measured on *BDT* and *DMcT* layers, respectively.

Figure 4-3a shows the current-noise PSD (at 95 Hz) versus bias voltage V_b graph measured on OT molecules using our noise imaging setup. As indicated with a fitting curve S_{fit} (black dashed line), the noise PSD was found to be approximately proportional to the square of the bias voltage, with small deviations from the fitting curve. Previous works suggested that the current noises in molecular wire junctions might be generated mainly by two different mechanisms: a tunneling-resistance fluctuation [18,19] and an electric-field fluctuation by a local-heating effect [13,20] (Figure 4-3b). Thus, the total current-noise PSD S_I (at a frequency *f*) in a molecular wire junction under a bias voltage V_b can be written like

$$(1) \qquad S_I(V_b) = S_{I,\text{resistance}}(V_b) + S_{I,\text{local heating}}(V_b)$$

where $S_{\mathrm{I,resistance}}$ and $S_{\mathrm{I,local\ heating}}$ are the noise PSD components from the *tunneling-resistance fluctuation* and *local heating effect*, respectively. The fluctuation of the tunneling resistance (R) in a molecular wire junction can be resulted from various origins such as the instability of the molecules-electrode bonding [18,19,21]. When the bias voltage V_{b} on a molecular wire junction is rather small (Figure 4-3b(i)), the current-noise PSD $S_{\mathrm{I,resistance}}$ by the tunneling-resistance fluctuation is reported to be proportional to the ${V_{\mathrm{b}}}^2$ like

$$S_{\mathrm{I,resistance}}(V_{\mathrm{b}}) \sim A_{\mathrm{r}} \times {V_{\mathrm{b}}}^2 \tag{2}$$

with the fitting parameter A_{r} [21]. On the other hand, as the applied bias voltage increases and reaches the energy of a molecular vibrational mode in the molecular wire junction, electrons tunneling through the junction can donate energies to the molecular wires to excite their vibrational modes (Figure 4-3b(ii)). The vibrationally-excited molecular wires relax to their ground states giving back the energies to the electron sea in the gold and Pt probes [20,22-24], increasing the kinetic energies of the electrons near the junction (Figure 4-3b(iii)). This effect is typically called as the local heating effect of a molecular junction [20,22-24]. The random electron motions enhanced by the local heating can induce the fluctuation of electric fields in the junction, generating current noises [13,20]. The noise PSD $S_{\mathrm{I,local\ heating}}$ from the local heating is usually small

compared with the $S_{\mathrm{I,resistance}}$ from the resistance fluctuation, and the $S_{\mathrm{I,local\ heating}}$ can reach a maximum value when the electron energy by the applied voltage corresponds to the energy of a molecular vibrational mode in the junction [25]. Thus, in the Figure 4-3a, the large component proportional to V_{b}^2 can be explained as the $S_{\mathrm{I,resistance}}$ generated by the tunneling-resistance fluctuation, while the small deviations from the fitting curve can be considered to show the $S_{\mathrm{I,local\ heating}}$ from the molecular vibrational modes [13]. Thus, from Eq. (1), the $S_{\mathrm{I,local\ heating}}$ can be written as,

$$S_{\mathrm{I,local\ heating}}(V_{\mathrm{b}}) \cong S_{\mathrm{I}}(V_{\mathrm{b}}) - A_{\mathrm{r}} \times V_{\mathrm{b}}^2 \tag{3}$$

This equation shows that the $S_{\mathrm{I,local\ heating}}$ can be estimated by fitting the measured S_{I} curve to the A_{r} x V_{b}^2 as a baseline and subtracting the fitting curve from the S_{I} curve. Further, in this work, we define the normalized noise PSD S_{n} like,

$$S_{\mathrm{n}}(V_{\mathrm{b}}) \equiv \frac{S_{\mathrm{I,local\ heating}}(V_{\mathrm{b}})}{S_{\mathrm{I}}(V_0)} = \frac{S_{\mathrm{I}}(V_{\mathrm{b}}) - S_{\mathrm{I,resistance}}(V_{\mathrm{b}})}{S_{\mathrm{I}}(V_0)} \sim \frac{S_{\mathrm{I}}(V_{\mathrm{b}}) - A_{\mathrm{r}} \times V_{\mathrm{b}}^2}{S_{\mathrm{I}}(V_0)} \tag{4}$$

where $S_{\mathrm{I}}(V_0)$ is the measured S_{I} at a fixed bias voltage V_0. Here, the $S_{\mathrm{I,local\ heating}}$ is normalized to the $S_{\mathrm{I}}(V_0)$, in order to remove the influence of the AFM probe size. In our system, a probe and an Au surface are connected by different numbers of molecular wires, depending on the probe size. Assuming that individual molecular wires incoherently transport

currents and generate electrical noises, the total noise PSD S_I through the probe should be approximately proportional to the size of the probe [17,21]. In this case, by normalizing the measured $S_I(V_b)$ by $S_I(V_0)$, we should be able to minimize the probe-size effect and obtain the information about the properties of molecular wires. Thus, the S_n should be very useful in identifying the intrinsic property of a molecular wire itself in the junction. More specifically, the S_n can be regarded to represent the efficiency of a molecular wire for the generation of $S_{I,local\ heating}$, when an electron passes through the molecular wire under a bias voltage V_b.

The molecular vibrational modes were identified by evaluating the peaks in the graph of the normalized PSD S_n. Figure 4-3c shows the graph of the S_n which was calculated from the S_I data in Figure 4-3a using Eq. (4) and V_0 = 200 mV. The results show peaks at V_b = 30, 76, 128 and 162 mV. Note that if we convert the peak voltage to the charge carrier energies by multiplying the peak voltage by a carrier charge e, the distribution of the peak energies matches well with the energies of well-known molecular vibrational modes on the OT molecules [13,26]. The corresponding molecular vibrational mode for each peak is marked in the graph. The identified molecular vibrational modes from the peaks are the Au-S stretching mode (ν(Au-S)), C-S stretching mode (ν(C-S)), C-C

stretching mode (ν(C-C)), and CH_2 out-of-plane wagging mode ($\gamma\omega(CH_2)$). The modes are known to have net dipole moments perpendicular to the gold-OT interface and thus easily interact with the tunneling electrons generating strong signals in the electrical vibrational-mode spectroscopy [26]. Interestingly, the intensity of the peak assigned to ν(C-C) mode is distinctively high compared with the other peaks. Previously, it was reported that the ν(C-C) mode can generate a dominant signal in the vibrational mode spectroscopy of alkanethiol molecules due to its peculiar vibrational feature favorable to the vibration mode-electron interactions [27], which is consistent with our observation. The results show that the analyses of electrical noises in a molecular wire junction can provide information about the vibrational modes of molecular wires in the junction. Our method provides a new way of the vibrational mode spectroscopy applicable to nanoscale materials and can be used for versatile basic researches and applications on nanoscale systems.

Figure 4-3d shows the averaged S_n graph obtained by averaging S_n graphs measured at 10 different positions on the OT layer using our noise microscopy. Here, the red line shows the averaged S_n values and the gray region shows the error band of one standard deviation. In the

graph, the peaks of ν(Au-S), ν(C-S), ν(C-C), and γω(CH_2) can be clearly identified, showing the high statistical reliability of our analysis method using the noise microscopy. The error band was quite thick near the peaks, presumably because the peak positions and intensities can be slightly different at different gold-OT junctions depending on the atomic configurations of Au-S contacts in the junctions [28].

Figure 4-3e shows the histogram of the peak positions in the S_n graphs measured on the OT layer. The V_b value at any local maximum of a S_n graph was identified as a peak position. The histogram well reproduced the results in the S_n graphs, confirming that the S_n spectrum can be used to measure the molecular vibrational modes on a molecular junction. The slight variations may come partly from some mechanical instability of contacts between molecular wires and the conducting probe. Previous works showed that, when the contact force between the probe and the sample is rather weak, the probe-sample contact can be unstable and the mechanical instability can generate the significant amount of mechanical noises [29]. As a matter of fact, we also found unstable noise signals presumably due to unstable junctions when the contact force is below 0.1 μN, while we could obtain reliable vibrational noise spectra with a rather large contact force from 1 μN as shown in Figure 4-3e.

Thus, we applied a 1 μN or larger contact forces during the measurements of noise maps presented in this study.

To demonstrate the general applicability of our noise analysis method for the investigation of molecular vibrational modes, we conducted the analysis on various molecular wires with different structures. Figure 4-3*f* and *g* show the averaged S_n graphs measured on *a BDT molecular layer* and *a DMcT molecular layer*, respectively. For both cases, the peak positions are in a good agreement with the reported vibrational modes of the molecules [23,28]. Comparing our results with previous reports on vibrational modes of the molecules [23,28], one can see that our analysis method allows us to observe all molecular vibration modes observable by the conventional spectroscopy methods. One of the advantage in our method is that the local heating induced by inelastic tunneling in a molecular junction always *increases* the current noises and, thus, the signals from the vibrational modes should be observed as *positive* peaks which are usually much easier to identify than other signals such as negative dips or inflection points in some conventional methods [1,2,13,26]. Figure 4-3*h* and *i* show the histograms of peak positions in the S_n graphs measured at the *BDT* and *DMcT* layers, respectively. The results show that S_n peaks were frequently observed near the molecular vibrational mode energies, showing the reliability of

our analysis.

4.5 Mapping of Molecular Vibrational Modes

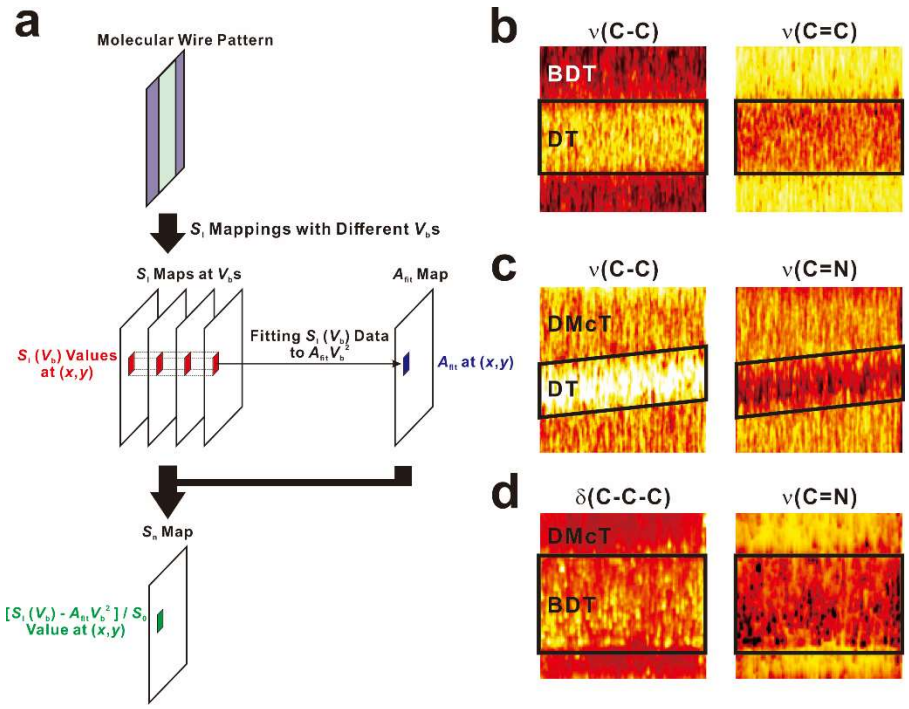

Figure 4-4 Mapping of molecular vibrational modes with a nanoscale resolution. (a) Schematic diagram showing the vibrational mode mapping method. (b) S_n maps measured on a sample patterned with DT and BDT molecules at *130 mV* (left) and *198 mV* (right) of bias voltages which correspond to the molecular vibrational modes of *C-C stretching mode* and *C=C stretching mode* , respectively. (c) S_n maps measured on a DT/DMcT sample with *130 mV* (left) and *182 mV* (right) correspond to the *C-C stretching mode* and *C=N stretching mode*, respectively. (d) S_n maps measured on a BDT/DMcT sample with *94 mV* (left) and *182 mV* (right) of bias voltages, which correspond to the *C-C-C bending mode* and *C=N stretching mode*, respectively.

Our vibrational noise spectroscopy method can be used to obtain a two-dimensional map of molecular vibrational modes on the patterns of molecular wires (Figure 4-4). Figure 4-4a shows a schematic illustration showing the method for the vibrational mode mapping. Here, we measured the normalized PSD S_n at a bias corresponding to a specific vibration mode energy on each location (x, y) in a desired region and utilized the data to form a map representing the molecular vibration mode. In brief, we first measured multiple (usually four or more) maps of S_I with different voltages (V_b s) in the same region of the molecular patterns. Then, the measured S_I (V_b, x, y) values at a location (x, y) (marked by a square) were fitted by the function of A_r x V_b^2 to obtain the fitting parameter $A_r(x, y)$ at the location. Then, $S_I(V_b, x, y)$ measured with a bias voltage corresponding to a specific vibration mode energy is subtracted by A_r x V_b^2, and it was divided by the current noise PSD values S_I at the 200 mV (S_0) to obtain the normalized noise PSD $S_n(V_b, x, y)$ at each location (x, y), forming the map of molecular vibration modes in the region.

Figure 4-4b shows the maps of normalized PSD S_n measured on a sample patterned with DT and BDT molecules at 130 mV (left) and 198 mV (right). The *130* and *198* mV corresponds to the molecular vibrational modes of *C-C stretching* and *C=C stretching*, respectively,

as marked in the images. The region of the DT molecules could be identified in a topography map measured along with the noise maps and is marked by a black square in the figures. In the left figure showing the C-C stretching mode, stronger signals were observed in the DT region, presumably due to the alkane chains in DT molecules. On the other hand, in the right figure representing a C=C mode, the BDT region appeared brighter, implying the existence of the C=C stretching mode in the BDT molecules. The results show that our analysis method can be used to obtain the distribution maps of molecular vibrational modes on the patterned molecular wires.

Figure 4-4*c* and *d* show the maps of S_n measured on a *DT/DMcT* and *BDT/DMcT* patterned molecular samples, respectively. We could observe the C-C stretching mode in the DT region and C=N stretching mode at DMcT region, in the Figure 4-4c. The observation implies the abundance of *C-C structure* and *C=N* structure in the *DT* and *DMcT* molecule, respectively. Similarly, in Figure 4-4d, we could observe the *C-C-C* and *C=N* molecular structure in the *BDT* and *DMcT* molecules, respectively. The results show that our noise microscopy-based strategy to identify molecular structures could be successfully applied to various molecular species with different molecular structures.

4.6 Summary

We have developed a strategy, named as “vibrational noise spectroscopy”, to identify and map vibrational modes of molecular wires on a solid substrate. In the strategy, a Pt-based conducting probe made a direct contact with a molecular-wire layer on a conducting substrate to measure current-noise PSDs. Interestingly, we found that the bias voltage applied to the Pt probe can stimulate specific molecular vibrational modes of the molecular wires, and the noise PSDs increased suddenly when the voltage reaches a vibrational mode energy of measured molecular wires. Thus, analyzing noise-voltage spectra, we could identify the vibrational modes of molecular wires on a gold substrate. Further, the VNS strategy could be utilized to map vibrational mode distributions on the patterns of different molecular wires. In addition, we found that the mapping data can be further analyzed to quantitatively estimate the density of a specific vibration mode in different molecular-wire layers. Since the VNS method enables the nanoscale mapping of molecular vibrational modes under ambient conditions, it can be a simple but powerful tool for basic researches and applications in various areas of nanoscale electronics and material analyses.

4.7 References

[1] Aouani, H.; Šípová, H.; Rahmani, M.; Navarro-Cia, M.; Hegnerová, K.; Homola, J.; Hong, M.; Maier, S. A. *ACS Nano* **2013,** *7*, 669–675.

[2] Adkins, C. J.; Phillips, W. A. *J. Phys. C: Solid State Phys.* **1985,** *18*, 1313-1346.

[3] Hansma, P. K. *Tunnelling spectroscopy: capabilities, applications, and new techniques*; Plenum: New York, 1982.

[4] Stockle, R. M.; Suh, Y. D.; Deckert, V.; Zenobi, R. *Chem. Phys. Lett.* **2000,** *318*, 131–136.

[5] Pettinger, B.; Ren, B.; Picardi, G.; Schuster, R.; Ertl, G. *Phys. Rev. Lett.* **2000,** *92*, 096101.

[6] Hapala, P.; Temirov, R.; Tautz, F. S.; Jelínek, P. *Phys. Rev. Lett.* **2014,** *113*, 226101.

[7] Sonntag, M. D.; Pozzi, E. A.; Jiang, N.; Hersam, M. C.; Van Duyne R. P. *J. Phys. Chem. Lett.* **2014,** *5*, 3125–3130.

[8] Poliani, E.; Nippert, F.; Maultzsch, J. *Phys. Status Solidi B* **2012,** *249*, 2511–2514.

[9] Huang, T.-X.; Huang, S.-C.; Li, M. H.; Zeng, Z.-C.; Wang, X.; Ren, B. *Anal. Bioanal. Chem.* **2015,** *407*, 8177–8195.

[10] Ochs, R.; Secker, D.; Elbing, M.; Mayor, M.; Weber, H. B. *Faraday Discuss.* **2006,** *131*, 281–289.

[11] Clément, N.; Pleutin, S.; Seitz, O.; Lenfant, S.; Vuillaume, D. *Phys. Rev. B* 2007**,** *76*, 205407.

[12] Kim, Y.; Song, H.; Kim, D.; Lee, T.; Jeong, H. *Acs Nano* **2010,** *4*, 4426–4430.

[13] Tsutsui, M.; Taniguchi, M.; Kawai, T. *Nat. Commun.* **2010,** *1*, 138.

[14] Tsutsui, M.; Taniguchi, M.; Kawai, T. *Nano Lett.* **2008,** *8*, 3293-3297.

[15] Engelson, M. *Modern spectrum analyzer theory and applications*; Artech House: Norwood, 1984.

[16] Scaini, D.; Castronovo, M.; Casalis, L.; Scoles, G. *Acs Nano* **2008,** *2*, 507–515.

[17] Cho, D.; Lee, H.; Shekhar, S.; Yang, M.; Park, J. Y.; Hong, S. *Sci. Rep.* **2017,** *7*, 43411.

[18] Xiang, D.; Lee, T.; Kim, Y.; Mei, T.; Wang, Q. *Nanoscale* **2014,** *6*, 13396–13401.

[19] Sydoruk, V. A.; Xiang, D.; Vitusevich, S. A.; Petrychuk, M. V.; Vladyka, A.; Zhang, Y.; Offenhausser, A.; Kochelap, V. A.; Belyaev, A. E.; Mayer, D. *J. Appl. Phys.* **2012,** *112*, 014908.

[20] D'Agosta, R.; Sai, N.; Ventra, M. D. *Nano Lett.* **2006,** *6*, 2935-2938.

[21] Kogan, S. *Electronic noise and fluctuations in solids*; Cambridge University Press: Cambridge, 1996.

[22] Huang, Z.; Chen, F.; D'agosta, R.; Bennett, P. A.; Di Ventra, M.; Tao, N. *Nat. Nanotechnol.* **2007,** *2*, 698–703.

[23] Tsutsui, M.; Taniguchi, M. *J. Appl. Phys.* **2013,** *113*, 084301.

[24] Ward, D. R.; Corley, D. A.; Tour, J. M.; Natelson, D. *Nat.* Nanotechnol. **2011,** *6*, 33–38.

[25] Safonov, S. S.; Savchenko, A. K.; Bagrets, D. A.; Jouravlev, O. N.; Nazarov, Y. V.; Linfield, E. H.; Ritchie, D. A. *Phys. Rev. Lett.* **2003,** *91*, 136801.

[26] Wang, W.; Lee, T.; Kretzschmar, I.; Reed, M. A. *Nano. Lett.* **2004,** *4*, 643-646.

[27] Okabayashi, N.; Konda, Y.; Komeda, T. *Phys. Rev. Lett.* **2008,** *100*, 217801.

[28] Lin, L.-L.; Wang, C.-K.; Luo, Y. *ACS Nano* **2011,** *5*, 2257–2263.

[29] Lee, M. H.; Hwang, C. S. *Nanoscale* **2011,** *3*, 490–502.

Chapter 5

Conclusions

In this dissertation, electrical-noise phenomena in a variety of nanoscale electronic systems were investigated using variations of a noise microscopy method.

Firstly, we developed “photoconductive noise microscopy” to image electronic traps distributed on a perovskite solar-cell film. Using the method, we could quantitatively image the distributions of ‘trap densities’, ‘high-bias photocurrents’, and ‘short-circuit currents’ on solar cell films, simultaneously. The results show a large spatial variation of the trap density and local photocurrents. Significantly, detailed analyses revealed that the trap density has power-law relationships with the local photocurrents and short-circuit currents in the perovskite solar-cell film. The results imply the charge traps are a main factor determining the local performance of perovskite-based solar cells, presumably due to the trap-induced photocarrier recombination mechanism.

Secondly, we conducted comparative studies on electrical noises in various species of molecular wires via a noise microscopy on a patterned molecular wires. Importantly, analysis results of our noise

mapping data implies that noises in metal-molecular wires-metal channels could be mainly originated from molecular wire-metal bond fluctuations. Furthermore, spectral analyses of noise maps indicated that such bond fluctuations could occur more frequently in rod-shaped molecular wires than in ring-shaped ones.

Lastly, we report the development of a new vibrational spectroscopy named as “vibrational noise spectroscopy (VNS)”. In the VNS, a Pt nano-probe made a direct contact with molecular wire patterns to measure the electrical noise spectra from the molecular wires. The measure noise spectra were analyzed to identify and map the molecular vibration modes of the molecular wires. We found that when the applied bias to the Pt nano-probe matched with a vibrational mode energy of the molecular wires, the vibrational mode could be stimulated resulting in enhanced electrical noises. Thus, by analyzing noise-voltage spectra, we could identify molecular vibrational modes of the measured molecular wires. Further, the VNS could be used to image and even quantitatively estimate the distribution of a specific vibrational mode on the patterns comprised of different molecular wires.

The results should contribute to broadening the understanding of noise phenomena in nanoscale electronic systems. Further, reported noise analysis methods such as VNS are expected to be widely utilized

as a useful tool for basic researches on nanoelectronics in general.

Chapter 6

Abstract in Korean

초록

노이즈 현미경법으로 조사한 다양한 나노 구조의 전기적 잡음 특성 및 그 특성과 나노 구조의 다른 물리적 성질들의 관계

전기적 잡음이란 전자 재료 또는 장치에서 발생하는 전기 신호의 무작위한 변동을 일컫는다. 원하지 않는 전기적 잡음의 발생은 신뢰할 수 있는 나노 크기 전자 장치의 개발을 위하여 필히 해결해야 하는 문제이다. 또한, 전기적 잡음의 측정 및 분석은 측정된 시스템에 대하여 다른 방법으로는 얻지 못하는 중요한 정보를 제공할 수 있는 것으로 알려져 있으며, 따라서 전기적 잡음에 대한 연구는 나노 전자 시스템에 대한 근본적인 이해를 위하여 꼭 필요하다. 본 연구에서는 전도성 원자간력 현미경에 기반한 주사 잡음 현미경법의 다양한 변형을 통

하여 조사한 다양한 나노 구조에서 발생하는 전기적 잡음 현상에 대하여 논의 할 것이다.

먼저, 국소적 전기적 잡음원들이 페로브스카이트 물질 기반 태양 전지의 성능에 미치는 영향에 대하여 논의 할 것이다. 이를 위하여, 태양 전지 박막에 분포하는 전기적 잡음원들의 밀도를 정량적으로 이미징하기 위하여 광전도 주사 잡음 현미경법을 개발하였다. 흥미롭게도, 잡음원의 밀도는 태양 전지 박막의 국부 광전류와 지수 함수 관계를 가지고 있는 것을 관찰하였으며, 전기적 잡음원의 분포가 페로브스카이트 기반 태양 전지의 성능을 결정짓는 핵심 요소임을 밝혔다.

다음으로, 분자 전자 소자에서 발생하는 전기적 잡음에 관하여 논의 할 것이다. 분자 소자의 저항에서 발생하는 전기적 잡음의 크기는 저항의 제곱에 비례하는 것을 관찰하였으며, 나노 크기의 분자 전자 소자에서 발생하는 전기적 잡음의 주요원인은 분자−금속 간 결합의 무작위적인 변동임을 밝혔다.

마지막으로, 전기적 잡음 분석을 통한 새로운 진동 분광법의 개발에 관하여 논의 할 것이다. 이 방법에서는 전도성 원자간력 현미경에 설치된 백금 탐침을 사용하여 전도성 기판

위에 증착된 분자에서 생성되는 전기적 잡음을 측정한다. 백금 탐침에 인가된 전압이 측정된 분자의 특정 진동 모드의 에너지와 일치할 때 해당 진동 모드가 자극되어 전기적 잡음이 증가하는 것을 관찰하였다. 이 원리를 이용하여, 전기적 잡음-전압 스펙트럼을 분석함으로써 측정된 분자의 진동 모드를 식별 할 수 있었다. 또한, 이 방법은 다양한 분자로 구성된 패턴 위에서 특정한 진동 모드의 분포를 정량적으로 이미징 하는데 사용될 수도 있었다.

주요어: 전기적 잡음, 나노 전자소자, 나노 물질, 원자간력 현미경, 전기적 잡음 이미징, 전하 트랩, 진동 분광법

학번: 2013-30922